JOURNAL OF AIRCRAFT
Vol. 53, No. 4, July-August 2016

# Grid Quality and Resolution Effects for Aerodynamic Modeling of Ram-Air Parachutes

Mehdi Ghoreyshi*
*U.S. Air Force Academy, Colorado Springs, Colorado 80840*
Keith Bergeron†
*U.S. Army Natick Research, Development, and Engineering Center, Natick, Massachusetts 01760*
and
Jürgen Seidel,‡ Andrew J. Lofthouse,§ and Russell M. Cummings¶
*U.S. Air Force Academy, Colorado Springs, Colorado 80840*

DOI: 10.2514/1.C033391

**This work provides an overview of the grid quality and resolution effects on the aerodynamic modeling of ram-air parachute canopies. The computational-fluid-dynamics simulations of this work were performed using the Cobalt flow solver, which is a three-dimensional code, but it was run in a two-dimensional mode for canopy sections with open and closed inlets. Previous simulation results of these geometries showed that grid independence is achieved for the closed and open airfoils with grids containing around half a million and 2 million cells, respectively. Previous grids were either hybrid with prismatic layers near the walls or multiblock structured using algebraic grid generators. The results presented in this work show that grid independence of both geometries can be achieved with much coarser grids. These grids, however, were generated with good smoothness, wall orthogonality, and skewness qualities. The results show that the grid quality value is mainly related to the grid smoothness and does not depend on the grid skewness or the wall orthogonality. Although a smooth grid improves the quality value, and therefore the solution convergence, it does not always lead to an accurate solution. For example, the unstructured grids with anisotropic cells near the wall have very good grid quality; however, they have the worst accuracy among all grids considered because of the poor skewness at the walls. The results also showed that, in comparison to the closed inlets, the open geometry solutions are less sensitive to the initial grid spacing and number of constant spacing layers at the outside airfoil walls. Finally, the open inlet solutions do not change with the inside airfoil grid resolution and type.**



## Nomenclature

| | | |
|---|---|---|
| $a$ | = | speed of sound, m/s |
| $C_D$ | = | drag coefficient, $D/q_\infty S$ |
| $C_L$ | = | lift coefficient, $L/q_\infty S$ |
| $C_p$ | = | pressure coefficient, $(p - p_\infty)/q_\infty$ |
| $c$ | = | mean aerodynamic chord, m |
| $D$ | = | drag force, N |
| GQ | = | grid quality |
| GR | = | growth rate in the viscous layer |
| $L$ | = | lift force, N |
| $l$ | = | far-field distance away from the airfoil, m |
| $M$ | = | Mach number, $V/a$ |
| $N_s$ | = | number of layers of constant spacing normal to all viscous walls |
| $p$ | = | static pressure, Pa |
| $p_\infty$ | = | freestream pressure, Pa |
| $q_k^i$ | = | $k$th grid quality metric at $i$th cell |
| $q_\infty$ | = | $\rho V^2/2$, dynamic pressure, Pa |
| $Re$ | = | Reynolds number, $\rho V c/\mu$ |
| $S$ | = | planform area, m$^3$ |
| $t$ | = | time, s |
| $t^*$ | = | normalized time, $tV/c$ |
| $V$ | = | freestream velocity, m/s |
| $x$, $y$, $z$ | = | grid coordinates |
| $y^+$ | = | nondimensional wall distance |
| $\alpha$ | = | angle of attack, deg |
| $\Delta_{s1}$ | = | initial spacing at all viscous walls |
| $\eta, \zeta, \xi$ | = | grid orientation vector |
| $\mu$ | = | air viscosity, kg/(m · s) |
| $\rho$ | = | air density, kg/m$^3$ |

Presented as Paper 2015-0407 at the 53rd AIAA Aerospace Sciences Meeting, 2015, Kissimmee, FL, 5–9 January 2015; received 6 February 2015; revision received 24 September 2015; accepted for publication 1 October 2015; published online 21 December 2015. 

*Senior Aerospace Engineer, High Performance Computing Research Center. Senior Member AIAA.

†Senior Research Aerospace Engineer. Senior Member AIAA.

‡Senior Aerospace Engineer, High Performance Computing Research Center. Senior Member AIAA.

§Director, High Performance Computing Research Center. Senior Member AIAA.

¶Professor of Aeronautics, High Performance Computing Research Center. Associate Fellow AIAA.

## I. Introduction

THE accuracy and expediency of computational fluid dynamics (CFD) solutions depend not only on the underlying numerical methods but also on the grid-generation process in which the computational domain is discretized into distinct subdomains. These subdomains are called cells or grid blocks. The computational grids should exactly represent the geometry of the problem of interest; however, truncation and machine roundoff errors are still present in the numerical solutions of partial or ordinary differential equations [1]. These errors depend on the grid size such that, for a finer grid, the truncation errors decrease, but the rounding errors will increase. Finally, inaccurate interpolation of the discrete solutions between grid blocks will increase the numerical error.

Uniform grids have many advantages over nonuniform grids, including more accuracy and faster convergence [2]. However, to resolve boundary-layer and wake regions in viscous flows, a uniform grid approach would require a very large number of grid points, which increases the computational cost. Practical turnaround times for obtaining a CFD solution and availability of computer resources would limit the uniform grid applicability for three-dimensional (3-D) problems. The total number of grid points, and therefore computational cost, can be reduced by using a nonuniform grid approach, in which the grid points are clustered near the regions of interest and are coarsely distributed elsewhere. These nonuniform cells can sometimes lead to grids of locally poor quality that will increase the computational solution error [3]. The performance of numerical methods can be significantly reduced even if just a few low-quality cells are present [4].

Grid-generation efforts can be traced back to the 1960s. Since then, many grid-generation methods have been proposed, such as conformal mapping, algebraic construction, partial differential equation solutions (elliptic, hyperbolic, and parabolic equations), Delaunay, advancing-front, and many others [5]. These methods have been used to generate structured (ST) and/or unstructured (UNSTR) grids over simple to complex geometries. Each method leads to a different grid quality for a given geometry. Additionally, although some grid-generation methods could be fast and even automated, others are a time-consuming manual process.

Conformal mapping is the simplest method of structured grid generation, in which the computational domain is mapped onto a rectangular region. Although the method is simple and efficient and creates very high-quality cells, it is practical only for simple two-dimensional problems. To create a smooth structured grid, elliptic grid generators can be used, which involve the numerical solution of inhomogeneous elliptic partial differential equations [6]. Grid smoothness can help reduce the truncation error and improve the accuracy. A disadvantage of the elliptic grid generation is the limited control over the interior grid points. Algebraic methods have also been used to create structured grids. These methods use algebraic transformation and an interpolation scheme to distribute grid points from a discrete set of data [7]. In comparison to elliptic grid generators, algebraic methods require much less computational effort and have better control over grid point locations, but the grid may not be as smooth as an elliptic grid. To improve the interior grid over complex geometries, the multiblock strategy has been proposed, in which the computational domain is divided into several smaller subdomains (block), and then separate grids are generated for each block [8]. Each block can initially be meshed by an algebraic method, and then an elliptic solver is used to smooth the grids.

Although structured grids offer higher accuracy, simplicity, and easy data access compared to an unstructured grid, unstructured grids (using tetrahedra cells) are more popular for complicated geometries [9]. Delaunay and advancing-front methods are the most popular colored tetrahedral (triangular in two-dimensional geometries) grid generators. The advancing front creates the cells one by one, starting from the domain boundary and by marching a front toward the interior [10]. The front refers to the cells that meet ungridded domains; the front will eventually vanish when the grid is completed. The advancing-front approach will have the best-quality cells at the boundaries and the worst cells where the front collides with itself [10]. Therefore, this grid generator is very helpful for modeling inviscid or laminar flows over solid walls. The advancing-front method can even be used to create quadrilateral cells; however, the interior cells could have low quality, or the grid may not be completed for a complex geometry. Typical Delaunay grid generators start from a boundary discretization. New points and triangular cells are then added to satisfy a particular connectivity. The method maximizes the minimum angle of all triangles to avoid sharp and distorted cells wherever possible [11]. Delaunay grid generators, unlike the advancing-front method, have the worst cells at the domain boundary and the best cells in the interior [10]. Therefore, the Delaunay and the advancing front approaches are often combined to use the advantages of both methods.

Unstructured grids are not effective when localized regions of high gradients appear in the flow, such as boundary layers [12]. Hybrid grid generators and anisotropic tetrahedral extrusion are commonly used to treat boundary layers in unstructured grids. The first step of a hybrid approach is the triangulation of the computational domain and then placing prismatic (quadrilaterals in two-dimensional geometries) cells near boundary surfaces. The prismatic cells are typically created using an advancing layer scheme. In such a grid, the outside boundary nearly has isotropic tetrahedral cells [13]. A disadvantage is that prismatic cells may have poor quality near sharp edges. An anisotropic tetrahedral extrusion creates triangular cells in a layer-by-layer fashion with the extrusion direction normal to the surface [12]. The method begins with an isotropic tetrahedral grid (generated by Delaunay and/or advancing-front methods), and tetrahedra on surfaces are then subdivided into anisotropic cells for a user-specified number of layers [14]. However, this approach might create extremely stretched tetrahedra cells near the walls, which impact the accuracy of computations.

At the U.S. Air Force Academy, the hybrid grid approach has been successfully used for a number of years for CFD simulation of many fighter aircraft [15–18]. These grids have structured cells near solid surfaces and unstructured cells elsewhere. Specifically, an inviscid tetrahedral grid is generated using the ANSYS ICEM-CFD code. This grid will then be used as a background grid by the grid generator TRITET [19,20], which builds prism layers using a frontal technique. TRITET rebuilds the inviscid grid while respecting the size of the original inviscid grid from ICEM-CFD. More recently, the authors of this work used this hybrid grid approach for prediction of aerodynamic characteristics of a ram-air parachute [21,22]. The grid-sensitivity study showed that solutions are very sensitive to the grid quality and size for the airfoils/wings with an open inlet. For example, the airfoil solutions became grid-independent for the hybrid grids that have more than 1.7 million cells. That brings to mind a question of whether another grid generator could produce similar predictions to the hybrid fine grids, but at a much lower computational cost.

The objectives of the work presented here are twofold: 1) to assess the grid resolution and find coarse grids that can have comparable results to the fine grids, and 2) to enhance the understanding of the relationship between grid quality and the solution accuracy and convergence.

The following assumptions and conditions were included for the simulations.

1) Only two-dimensional airfoils and flows were considered.

2) Flow calculations were performed using the commercial code Cobalt, a cell-centered, finite volume, unstructured flow solver.

3) Turbulence contributions were included using the Spalart–Allmaras (SA) model.

The two-dimensional and SA turbulence model constraints necessarily limit extrapolation of the results to three-dimensional parachute configurations, which exhibit massively separated flows. However, the restrictions were imposed to serve as a baseline to reduce the number of parameters being varied within the study while preserving key attributes that have been extrapolated to engineering problems. For example, the grid quality metrics that were used focused on geometric information such as smoothness and skewness. Ultimately, the results of this work are intended to refine the guidelines applied to CFD modeling of ram-air parachutes.

## II. Computational-Fluid-Dynamics Solver

This study uses the commercial flow solver Cobalt, which solves the unsteady, three-dimensional, compressible Navier–Stokes equations in an inertial reference frame. Arbitrary cell types in two or three dimensions may be used; a single grid therefore can be composed of different cell types [23]. In Cobalt, the Navier–Stokes equations are discretized on arbitrary grid topologies using a cell-centered finite volume method. Second-order accuracy in space is achieved using the exact Riemann solver of Gottlieb and Groth [24] and least-squares gradient calculations using QR factorization. To accelerate the solution of the discretized system, a point-implicit method using analytic first-order inviscid and viscous Jacobians is used. A Newtonian subiteration method is used to improve the time accuracy of the point-implicit method. Tomaro et al. [25] converted the code from explicit to implicit, enabling Courant–Friedrichs–Lewy numbers as high as $10^6$. In Cobalt, the computational grid can be divided into group of cells, or zones, for parallel processing, where high performance and scalability can be achieved even on thousands of processors [26]. Some available turbulence models in Cobalt are the Spalart–Allmaras (SA) model [27], Spalart–Allmaras with rotation correction (SARC) [28], and delayed detached-eddy simulation with SARC [29].

Cobalt checks the grid quality and reports a score; this score is directly related to a particular part of the second-order accurate spatial operator inside Cobalt [30]. Specifically, consider a bounding face of a given cell. Various fluid quantities (e.g., density) are computed for the face using fluid data in the cell itself and central-difference gradients computed using data from all nearest neighbors of the given cell. If there is a local extremum at the face, then the central-difference gradient is replaced with a one-sided gradient for stability. This one-sided gradient omits, at the very least, data from the neighbor cell sharing the given face, and other neighbor cells may also need to be discarded [23]. The effect of each of these omissions is to add numerical dissipation, and the grid quality score is used to monitor the energy loss by tracking how many neighbor cells are turned off and their relative weight in the construction of one-sided gradients.**

The reported score is averaged over all the cells and ranges from zero to 100, such that the lower the grid score is, the more numerical dissipation is added to the solution (worse stability). Note that Cobalt's grid score involves the grid geometry information only and not the flow solution obtained on that grid. This means that the grid quality is a fixed number regardless of the angle of attack (AOA) and Mach number. Cobalt's User Guide [30] details that the high aspect ratio of cells (typically placed in the boundary layer) can cause the quality to suffer. Also, regions of high surface curvature can adversely impact grid quality. The grid quality will improve if a sufficient number of surface cells are used to accurately capture any geometric curvature.

## III. Grid Quality Measures

The relationship between the grid quality and solution accuracy will be investigated in this work. A priori grid quality metrics could provide some guidance of the grid before running it in CFD [31]. The grid quality mainly deals with the geometric information of the grid. Before examining the grid quality, one should check the grid for negative volume (or volumes below a threshold) and folded cells. These types of cells make a cell-centered flow solver impossible to iterate [32]. Typically, a high-quality grid is obtained by creating well-shaped cells (orthogonal structured cells or isotropic tetrahedra cells) with moderate smoothness. Therefore, most grid quality metrics indicate how much a grid cell deviates from its ideal shape.

The numerical predictions obtained on the grids could be used to improve the grid quality metrics [3]. One simple example is $y^+$ value at the walls. According to the gridding guidelines from the 2nd AIAA CFD High Lift Prediction Workshop [33], approximate initial spacing normal to all viscous walls should have $y^+$ values of approximately 1.0, 2/3, 4/9, and 8/27 for a coarse, medium, fine, and extra fine grid, respectively. In more advanced grid-generation methods, the solution errors are used to refine the grid in regions where the error is large.

Grid resolution and quality should be checked before running the grid in CFD. The grid resolution should be high enough to capture the flow physics. Mavriplis et al. [34], for example, have recommended a chordwise grid spacing of 0.1% of local chord (for a medium grid) at the wing leading and trailing edges. In the spanwise direction at the wing root and tip, a grid spacing of 0.1% of semispan was recommended. The grid dimension (size) at the wing trailing-edge base is recommended to be 8, 12, 16, 24 for a coarse, medium, fine, and extra fine grid, respectively. The grid resolution can be evaluated by sensitivity studies. The results become grid-independent if they show less than 3% difference from a 30% finer grid [35].

The grid quality is often measured for each cell from given information about the cell's aspect ratio and skewness. It is also desirable to have near-wall faces parallel to the wall. Additionally, the rate at which the grid spacing changes from one cell to another (grid smoothness) is important. Optimal grids have equilateral cells (equilateral triangles and squares) with a smooth change of dimensions through the domain [35]. Specifically, cell skewness should be kept relatively small because high aspect ratios would slow down the convergence. Finally, a spacing growth rate below 20% does not affect the solutions [35], but higher values affect the solution accuracy and convergence. The reader should note that these criteria might change from one solver to another. This is discussed later in this section.

Several other grid quality metrics have been suggested. Alter [36], for example, has described a grid quality metric for structured three-dimensional grids. This metric is defined by

$$\mathrm{GQ} = \frac{\bar{\theta}_{\min}\bar{\Theta}}{\bar{\epsilon}_{\max}} \tag{1}$$

where GQ denotes the grid quality ranging from zero to 1; $\bar{\theta}_{\min}$, $\bar{\Theta}$, and $\bar{\epsilon}_{\max}$ show deviations from orthogonality, straightness, and stretching, respectively. Best grid quality comes with $\mathrm{GQ} = 1$. Some examples of orthogonality, stretching, and straightness are shown in Fig. 1.

A grid quality metric based on the deviation from an ideal cell shape will probably invalidate most of anisotropic cells near the walls for viscous flows. On the other hand, these anisotropic cells are allowed in many flow solvers. In addition, for all cell-centered flow solvers, the quadrilateral faces should be planar; however, nonplanar faces are not an issue in most node-based solvers. McDaniel [32] therefore proposed that an independent grid quality should be provided from the viewpoint of each flow solver (cell-centered, node-based, and others). He then introduced grid quality metrics for the kCFD [37], which solves the unsteady, three-dimensional, compressible Reynolds-averaged Navier–Stokes equations on hybrid unstructured grids. Note that both Cobalt and kCFD code originated from the Air Vehicles Unstructured Solver (formally known as Cobalt60 [24]), which is a parallel, implicit, unstructured flow solver developed by the U.S. Air Force Research Laboratory. Both solvers have since been significantly modified. McDaniel then defined some grid quality metrics that are applicable to most cell-centered numerical algorithms and all cell types and take into account the fact that large-area faces have a larger flux contribution to the solution value in the cell.

## IV. Test Cases/Previous Results

The U.S. Department of Defense program to develop precision guided airdrop systems is known as the Joint Precision Airdrop System (JPADS), which is coordinated by the U.S. Army Natick Soldier Center. The JPADS uses round and ram-air parachutes (parafoils) for deceleration and control of the payload [38]. Different types of airfoil sections have been used for parafoils; initial ram-air canopy designs used the Clark-Y section, which has good lift-to-drag ($L/D$) characteristics for Reynolds numbers over several orders of magnitude ($500,000 < Re < 10^7$) [39,40]. Over the years, this airfoil shape has been modified for parachute applications to improve the lift-to-drag ratio; recent canopy designs are based on the airfoil sections used in glider design (for example, NASA LS1-0417 airfoil) [41]. In this work, the low-speed airfoil section of an actual parafoil is investigated. The airfoil considered here is a nonsymmetric airfoil that has a flat bottom surface. The flow around this airfoil has been studied by Ghoreyshi et al. [21] and Bergeron et al. [22] for open and closed inlets; the open and closed-inlet geometries are shown in Fig. 2.

Ghoreyshi et al. [21] performed the grid-independence study of both airfoils. These results are shown in Figs. 3 and 4. Closed airfoil grids are fully structured or hybrid; structured grids were generated using the multiblock techniques inside the commercial code of Pointwise V17.01.R3 released June 2013.†† Hybrid grids were generated using ICEM-CFD and the grid generator TRITET. All the grids labeled in Fig. 4 are of hybrid type.

Figure 3 shows that the solutions of structured medium (around 663,000 cells) and fine grids (around 3 million cells) match everywhere. The solutions of the hybrid medium grid (around 744,000 cells) are in close agreement with the medium and fine structured grids as well. The coarse structured grid (around 172,000 cells), however, only matches the solutions up to an angle of 6 deg; at

**Strang, W., Private Communication, June 2015.

††Data available online at http://www.pointwise.com [retrieved June 2015].

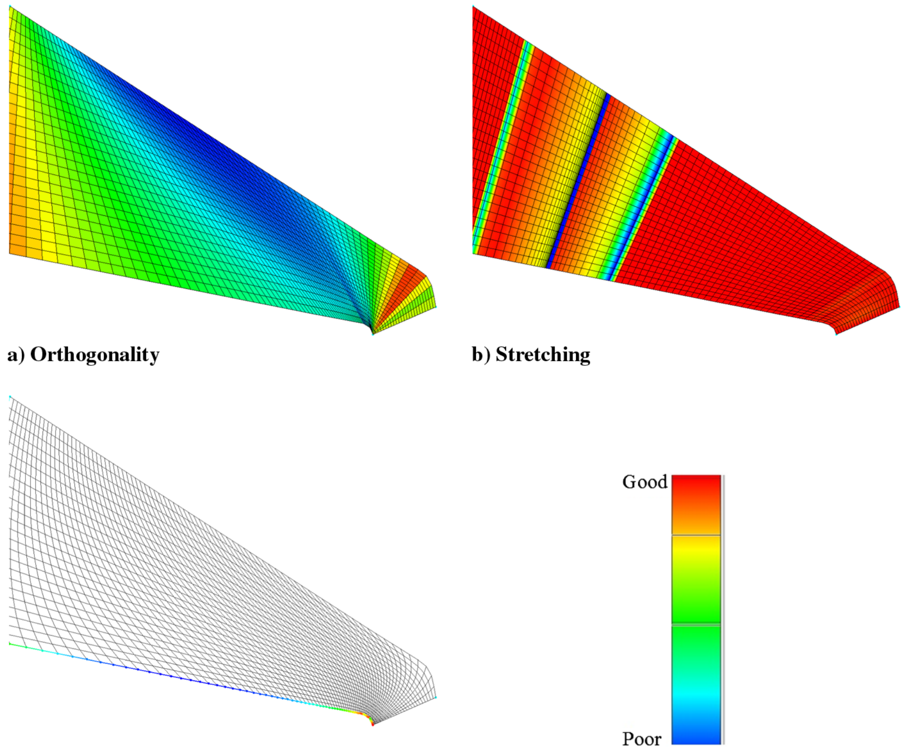


a) Orthogonality b) Stretching

c) Straightness

**Fig. 1 Orthogonality, stretching, and straightness examples for structured grids.**

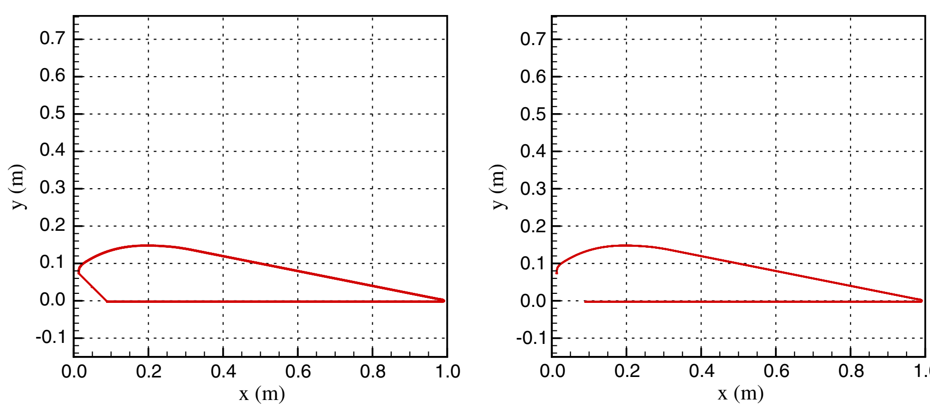


a) Closed inlet b) Open inlet

**Fig. 2 Airfoil geometries for the parachute cases.**

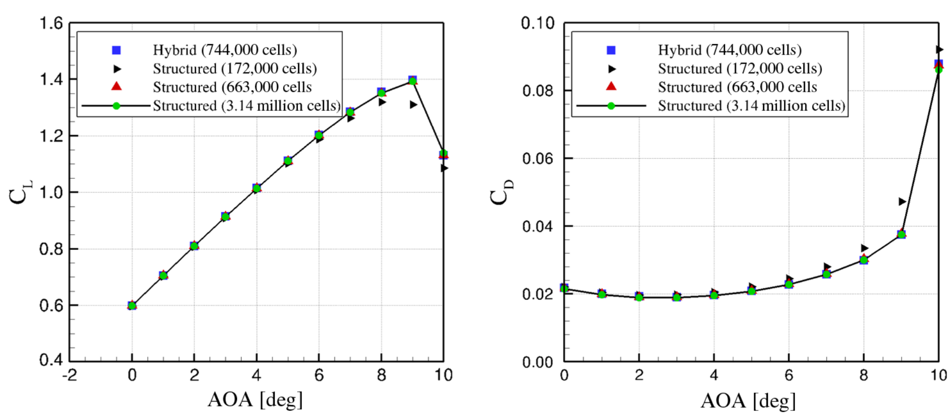


a) Lift coefficient b) Drag coefficient

**Fig. 3 Grid-independence study of the closed-inlet airfoil.**

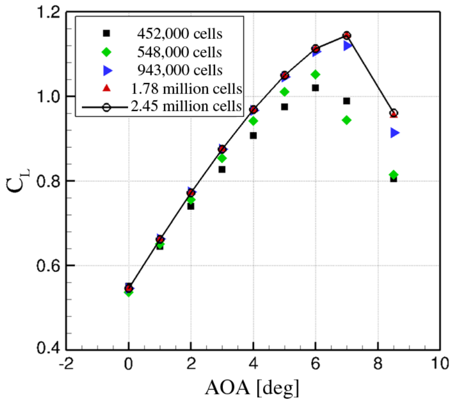


a) Lift coefficient

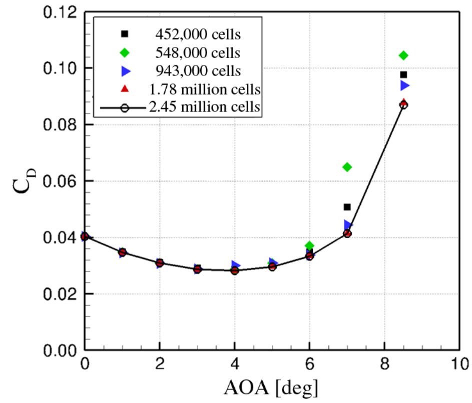


b) Drag coefficient

**Fig. 4 Grid-independence study of the open-inlet airfoil.**



higher angles, it predicts smaller lift and larger drag coefficients. The grid convergence index (GCI) values, which are a measure of the percentage difference between the computed solution and the asymptotic numerical solution, were estimated only for the coarse and medium grids at 8 deg angle of attack with an assumed safety factor of 1.25. The GCI indicates the amount of change in the computed solution that would result from additional grid refinement. The reader is referred to the work of Oberkampf and Roy [42] for more details of the grid convergence index. GCI values of the lift coefficient are 0.82% using the coarse grid and 0.0489% using the medium grid. For the drag coefficient, GCI values are 4.12 and 0.19% using the coarse and medium grid, respectively.

The closed airfoil is further investigated in this work. This geometry is used to determine if predictions of a low-resolution but high-quality grid can still match with the medium and fine grid data. The second goal is to relate the solution accuracy and convergence with grid parameters and quality metrics. All grids of this work were generated using Pointwise, and predictions were compared with solutions of the fine structured grid (containing 3 million cells). Cobalt reports an averaged grid quality of 99.74 in a range of zero to 100 for this fine grid.

Figure 4 shows that CFD solutions of the open-inlet airfoil largely depend on the grid resolution. Coarse and medium grids (containing around 452,000 and 548,000 cells) were generated from a low-density inviscid grid, and CFD data using these grids do not match with fine grid data (containing around 943,000, 1.78 million, and 2.45 million cells). Figure 4 shows that solutions do not change with grid density for the grids that have more than 1.78 million cells. GCI values of the lift coefficient at $\alpha = 8.5$ deg are 6.9 and 1.9% using grids containing 452,000 and 943,000 cells, respectively.

The coarse grids, with different grid-generation methods, are tested in Cobalt, and the results are compared to the Hfine grid (1.78 million cells) data in [21]. This grid has a Cobalt quality of 99.83. The gridding study is performed on both outside and inside domains. The effects of meshing on the solution accuracy and convergence are investigated.

## V. Results and Discussion

For the sake of convenience, the closed and open inlet grids are labeled “CG” and “OG,” respectively. All CFD simulations were performed using the Spalart–Allmaras (SA) turbulence model and were run on the Cray XE6 machine at the Engineering Research Development Center. The freestream velocity in all simulations was fixed at Mach 0.1, and the Reynolds number is $1.4 \times 10^6$ at standard sea-level conditions. The simulations were performed for an angle-of-attack sweep from zero to 10 deg with 1 deg increment. Wall boundary $y^+$ values shown in the results are the maximum values reported from the Cobalt code.

As noted in [21], the flow around an airfoil with an open leading edge is unsteady with large oscillations in lift and drag coefficients. Therefore, in all simulations of this work, second-order accuracy in time (i.e., unsteady), three Newton subiterations, and 20,000 iterations (ITER) with a normalized time step $\Delta t^*$ of 0.034 were used. The normalized time step defined as $t^* = Vt/c$ uses a length scale $c$ of 1 m and velocity $V$ of 34 m/s. The last 10,000 iteration values were time-averaged to obtain lift and drag coefficients.

All grids were run in Cobalt, and errors in the force coefficients from the predictions of fine grids are estimated. Specifically, the error norm of lift coefficient $C_L$, drag coefficient $C_D$, and lift to drag ratio $L/D$ is defined as

$$\text{err} = \frac{\sqrt{(1/N_i)\sum_{j=1}^{N_i}(y_j^{\text{New Grid}} - y_j^{\text{Fine Grid}})^2}}{|y_{\max}^{\text{Fine Grid}} - y_{\min}^{\text{Fine Grid}}|} \times 100 \tag{2}$$

where $y = [C_L, C_D, L/D]$; $N_i$ is number of angles of attack, which is 11 in this work. The error norm is also found for the maximum lift coefficient ($C_{L\,\max}$) as

$$\text{err2} = \frac{C_{L\,\max}^{\text{New Grid}} - C_{L\,\max}^{\text{Fine Grid}}}{C_{L\,\max}^{\text{Fine Grid}}} \times 100 \tag{3}$$

### A. Closed-Inlet Airfoil

A medium-size grid (named CG1) was generated with details given in Table 1. The grid was generated layer by layer using an elliptic extrusion method starting from the walls. The method stops when the new grid layer reaches a total height of 200 m. The outer edges of the cells, at the final layer, define the freestream boundary. The coarse grid used in [21] was also modified to have exactly the same number of grid points and spacings on the walls as the CG1 grid. This new grid (named CG2), however, was generated using a multiblock method with an algebraic grid generator applied to each block. CG2 grid details are also given in Table 1. Table 1 confirms that CG1 and CG2 grids have nearly equal number of cells. The overview of grids near the trailing edge is shown in Fig. 5.

Table 2 compares $y^+$, Cobalt grid quality, and the error norms on the CG1 and CG2 grids. Although both grids have approximately the same resolution, $y^+$, and grid quality, the errors from CG1 are one order of magnitude less than the CG2 grid. In more detail, Fig. 6 compares the lift and drag coefficients of CG1 and CG2 grids with the Structured Fine (SFine) grid data. The comparisons show that the CG1 grid perfectly matches with the SFine grid predictions; however, CG2 predictions do not match at all angles of attack. A question that arises is why these grids, both structured, with the same $y^+$, grid quality, and resolution, lead to different answers to the exact same problem.

Figure 7 shows the convergence histories of the density residual ($D\rho/Dt$) for the CG1 and CG2 grids as well as the SFine grid containing 3 million cells. Figure 8 also shows the time histories of lift and drag coefficients of the CG1 grid. Figures 7 and 8 show that

**Table 1 Closed grid details (in all grids GR = 1.1)**

| Grid | Type | Method | $\Delta_{s1}$ | $l/c$ | Number of cells |
|---|---|---|---|---|---|
| SFine | STR | Multiblock, algebraic | 1e − 5 | 50 | 3,141,000 |
| CG1 | STR | Normal extrusion, elliptic | 1e − 5 | 100 | 341,850 |
| CG2 | STR | Multiblock, algebraic | 1e − 5 | 100 | 324,570 |
| CG10 | STR | Normal extrusion, elliptic | 4e − 5 | 25 | 115,320 |
| CG11 | STR | Normal extrusion, elliptic | 4e − 5 | 50 | 120,900 |
| CG12 | STR | Normal extrusion, elliptic | 4e − 5 | 75 | 124,620 |
| CG13 | STR | Normal extrusion, elliptic | 4e − 5 | 100 | 128,340 |
| CG20 | STR | Normal extrusion, elliptic | 2e − 5 | 50 | 127,410 |
| CG21 | STR | Normal extrusion, elliptic | 1e − 5 | 50 | 133,920 |
| CG30 | UNSTR | Delaunay, anisotropic viscous layers | 4e − 5 | 50 | 101,894 |
| CG31 | UNSTR | Delaunay, anisotropic viscous layers | 2e − 5 | 50 | 114,970 |
| CG32 | UNSTR | Delaunay, anisotropic viscous layers | 1e − 5 | 50 | 128,564 |
| CG40 | Hybrid | Delaunay, 25 prismatic viscous layers | 1e − 5 | 50 | 55,324 |
| CG41 | Hybrid | Delaunay, 50 prismatic viscous layers | 1e − 5 | 50 | 77,754 |
| CG42 | Hybrid | Delaunay, 75 prismatic viscous layers | 1e − 5 | 50 | 100,842 |



both the CG1 and CG2 grids had approximately three orders of magnitude reduction in the density residual. The solutions converged to final values as the lift and drag variations are small (less than 0.1%). Figure 7 also indicates that both grids exhibit very similar convergence behavior after 5000 iterations. Because CG1 and CG2 have the same quality and resolution, a preliminary conclusion is that solution convergence in Cobalt is related to the grid quality and the resolution. The SFine grid quality in Cobalt is 99.74 slightly higher than CG1 and CG2; also it is a very high spatial resolution grid. As expected, Fig. 7 shows that the SFine grid has more residual drop than other grids.

Now, in attempting to answer the aforementioned question, the reader is referred again to the grid overviews shown in Fig. 5. Detailed visualization of the cells around the trailing edge reveals that CG1 has better wall orthogonality (straightness), smoothness, and skewness compared to CG2. Many cells in CG2 are highly skewed; furthermore, most grid lines are not orthogonal to the walls. However, Cobalt's overall grid quality is very similar for both grids. The grid quality plots of CG1 and CG2 (around the trailing edge) can also be seen in Figs. 9a and 9b. Note that white cells in the figures indicate high grid quality (above 99). Figure 9b shows that most CG2 cells in Cobalt have high quality, whereas they were expected to have low quality because of the poor flow alignment and skewness.

Grid smoothness, skewness, and the wall orthogonality values are also shown in Fig. 9. This figure shows that CG1 cells are well shaped with good smoothness and 90 deg wall angles. Comparing these plots with Cobalt grid quality pictures reveals that Cobalt grid quality is related to the grid smoothness but not the skewness or the wall orthogonality. Figure 10 shows the same correspondence for the cells near the leading edge. CG2 cells at the leading edge have slightly better smoothness than CG1, but it has highly skewed cells. Figure 10 shows that Cobalt's quality (at the leading edge) is better for CG2 compared to CG1 cells. This again confirms that Cobalt grid quality does not change with the skewness or wall orthogonality. This means that a high grid quality in Cobalt corresponds to good smoothness, which would improve the convergence, but it does not necessarily provide better accuracy. The flow solutions at the CG1 and CG2 grids will be presented later in this section.

Four new grids (CG10–CG13) were generated around the closed-inlet airfoil by the normal extrusion of the wall using an elliptic grid generator. The edge lengths of these grids are about half of the edges in CG1 and CG2 grids. All grids are structured and contain around

**Table 2 Closed grid solution details**

| | | | Error, % | | | |
|---|---|---|---|---|---|---|
| Grid | $y^+$ | Quality | $C_L$ | $C_D$ | $L/D$ | $C_{L\,\max}$ |
| SFine | 0.2677 | 99.79 | — — | — — | — — | — — |
| CG1 | 0.2663 | 98.62 | 0.1484 | 0.1276 | 0.2209 | 0.1183 |
| CG2 | 0.2339 | 98.81 | 1.1504 | 2.0752 | 5.6311 | −1.7914 |
| CG10 | 1.074 | 99.14 | 1.8921 | 2.9175 | 8.1312 | −1.7116 |
| CG11 | 1.074 | 99.15 | 1.7397 | 2.3424 | 5.0274 | −1.6729 |
| CG12 | 1.074 | 99.16 | 1.7155 | 2.2623 | 4.4330 | −1.6793 |
| CG13 | 1.074 | 99.19 | 1.7045 | 2.2196 | 4.0466 | −1.6824 |
| CG20 | 0.5336 | 99.12 | 1.0534 | 1.1167 | 2.7766 | −1.0541 |
| CG21 | 0.2663 | 98.99 | 0.8772 | 0.7775 | 2.2576 | −0.8549 |
| CG30 | 0.7260 | 99.83 | 0.3247 | 1.8036 | 4.3489 | 0.3532 |
| CG31 | 0.3642 | 99.71 | 4.3107 | 5.8003 | 3.6808 | 1.4514 |
| CG32 | 0.1796 | 99.55 | 3.5703 | 4.5855 | 2.9438 | 1.6056 |
| CG40 | 0.2663 | 98.55 | 5.2646 | 7.2829 | 7.8631 | −6.2807 |
| CG41 | 0.2663 | 98.97 | 1.0484 | 0.5219 | 1.6164 | −0.8507 |
| CG42 | 0.2663 | 98.94 | 0.5906 | 0.8316 | 2.1128 | −0.5507 |

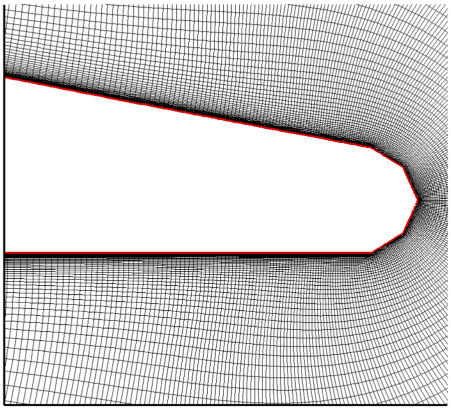

**a) CG1, structured (elliptic grid)**

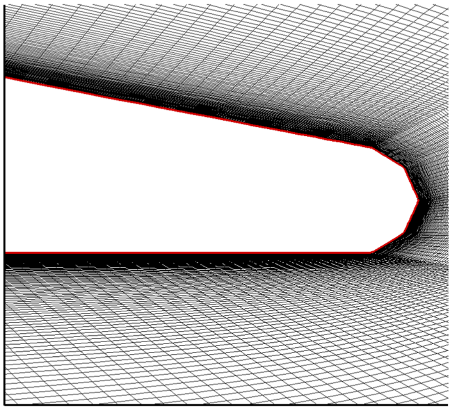

**b) CG2, multiblock (algebraic grid)**

**Fig. 5 CG1 and CG2 grids overview.**

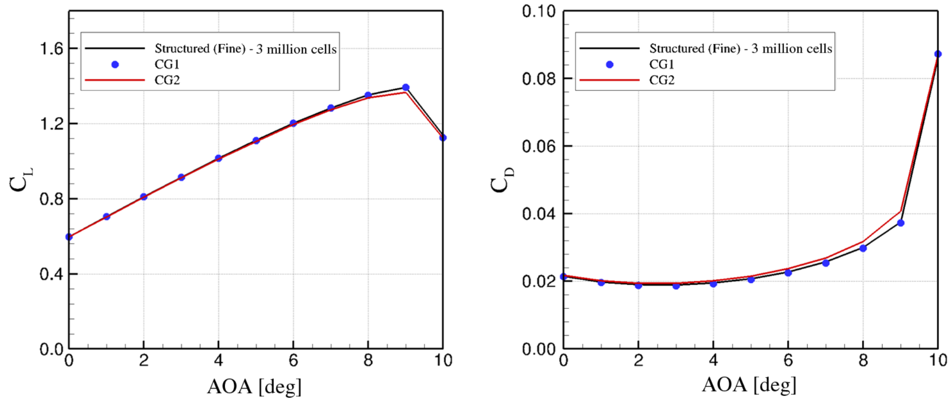


a) Lift coefficient

b) Drag coefficient

**Fig. 6 Lift and drag coefficients of CG1 and CG2 grids. The structured SFine grid is from [21].**

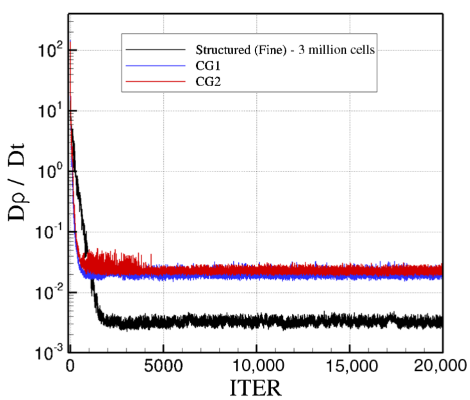


**Fig. 7 Density residual convergence ($D\rho/Dt$) of CG1 and CG2 grids, where $\rho$ and $t$ denote density and time, respectively. The structured SFine grid is from [21].**

120,000 cells. The near-wall grid spacing $\Delta_{s1}$ is $4 \times 10^{-5}$ m for these grids, which makes the overall $y^+$ near unity. The difference between these four grids is only due to the far-field length $l$; it varies from 25 to 100 chord lengths. Grid details and errors (from the SFine grid data) are given in Tables 1 and 2.

Figure 11a shows that CG10–CG13 grids have very similar convergence behavior, again, because these grids have a similar number of cells and quality. Figure 11a shows that the far-field length had no considerable effect on the convergence rate in Cobalt. Figure 11b also shows the error trends with far-field length for grids CG10–CG13. Increasing the far-field length above 50 chord lengths has no significant effect on the $C_L$, $C_D$, and $C_{L\ \max}$ errors. Figure 11b shows that $L/D$ predictions can be improved by making the far-field boundary bigger, but its impact becomes smaller above $50c$. For all subsequent grids, a far-field length of 50 chords will therefore be used.

CG20–CG21 grids were generated by similar grid-generation methods; however, the near-wall grid spacing $\Delta_{s1}$ varies in these grids. The convergence data of these grids (CG20–CG21) are shown in Fig. 12a, which shows the convergence improves as $y^+$ decreases from 1 to around 0.26 (CG11 in this figure has $y^+ = 1$). The solution accuracy is also improved with decreasing $y^+$, as shown in Fig. 12b. Figure 13 compares the lift and drag coefficient predictions of CG21 grid ($y^+ = 0.2663$ and containing 134,000 cells) with predictions from CG1 ($y^+ = 0.2663$ and containing 341,000 cells). The results show that CFD data of the coarse grid match very well with the medium grid data. Note that CG1 data also match with CFD data of the SFine grid. These results show that a grid size of around 134,000 cells and $y^+$ of 0.26 with well-shaped cells will match the fine data of [21].

Three unstructured grids (CG30–CG32) were also considered; these grids were generated by the Delaunay tetrahedralization and have anisotropic cells near the wall with a growth rate of 1.1. These grids are very similar, except that they have different initial spacing near the wall. Grid details and errors are given in Tables 1 and 2. These grids have around 115,000 cells and have grid quality above 99. Figure 14 compares CG21 (structured) with the CG32 (unstructured). The anisotropic cells near the wall can be seen in this figure. Note that anisotropic tetrahedral layers are not constant everywhere; the local extrusion at each point would stop if the cell size become close to the size of outside isotropic cells.

Figure 15 compares the Cobalt quality plot of CG32 with the Pointwise skewness quality picture of CG32. Figure 15b shows that the cells near the wall are extremely skewed, but Cobalt considers these cells high-quality ones because of the good grid smoothness. The convergence histories of CG1, CG21, and CG32 are plotted in Fig. 16. Despite having a poor skewness near the wall, CG32 has very

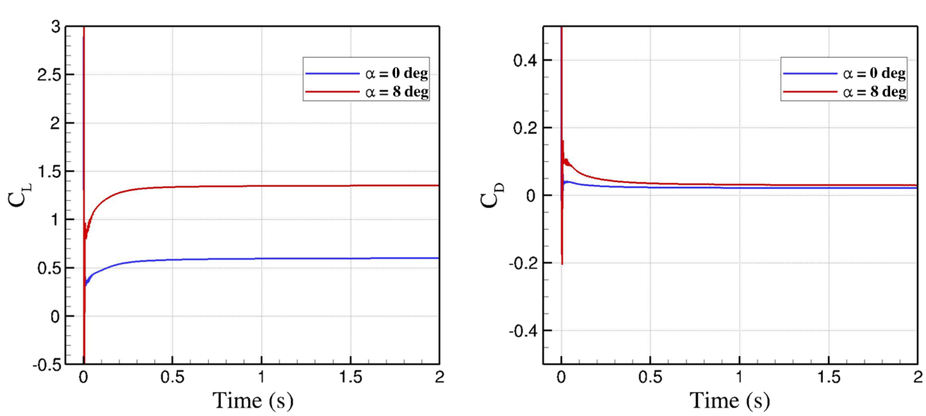


a) Lift coefficient

b) Drag coefficient

**Fig. 8 Convergence plots of CG1 grid at zero and 8 deg angles of attack.**

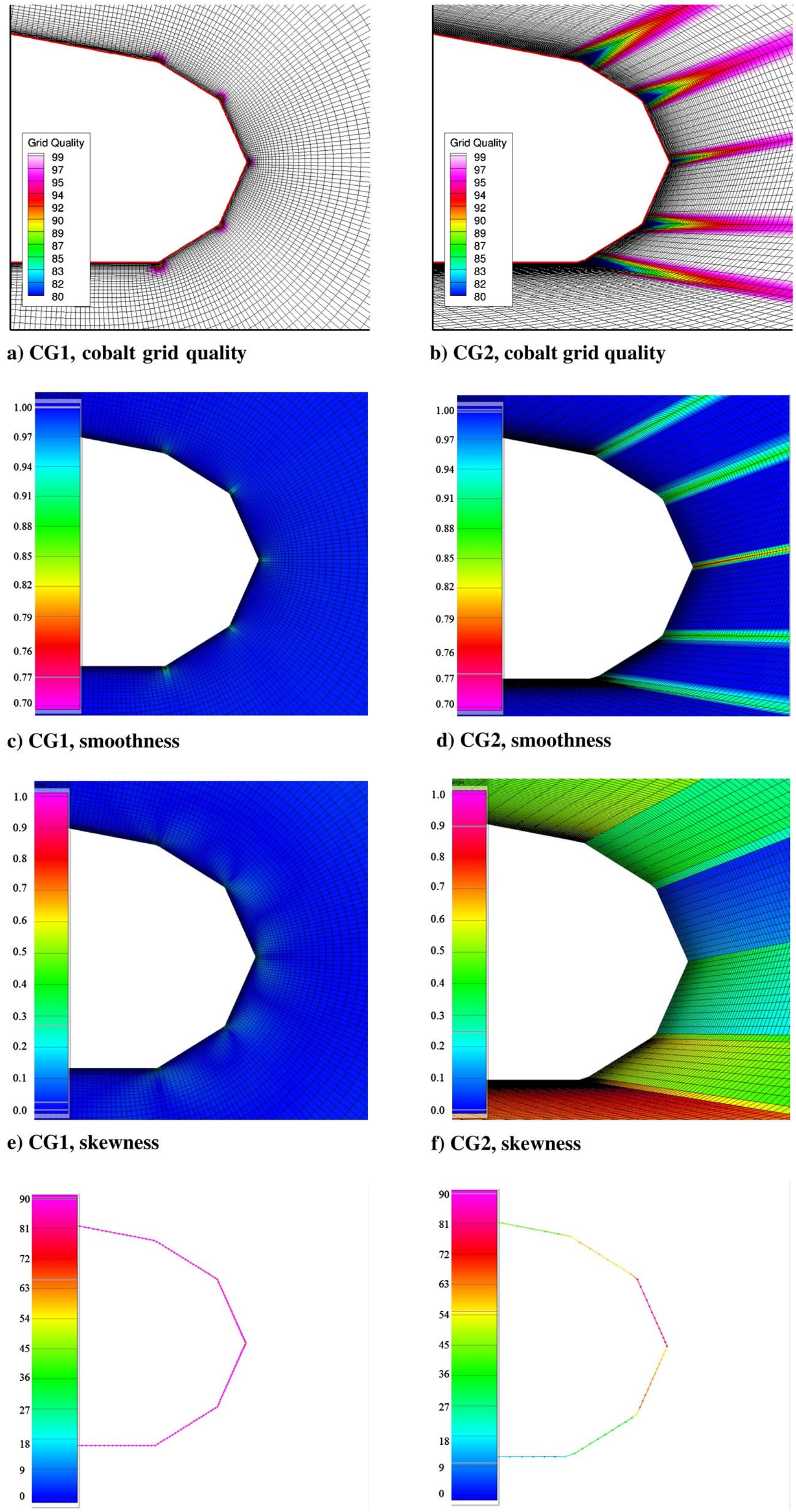


**a) CG1, cobalt grid quality** **b) CG2, cobalt grid quality**

**c) CG1, smoothness** **d) CG2, smoothness**

**e) CG1, skewness** **f) CG2, skewness**

**g) CG1, wall orthogonaliy (deg)** **h) CG2, wall orthogonaliy (deg)**

**Fig. 9 Cobalt grid quality relationship with grid geometry; grid is around trailing edge. In Figs. 9a and 9b, the white cells have the highest quality.**

similar convergence behavior to CG21, which is a structured grid. This again confirms that Cobalt convergence does not change much with the skewness quality. CG1 has better convergence than the other grids because it has a high resolution compared with CG21 and CG32.

Although CG32 and CG21 have similar quality and convergence, Table 2 shows that CG32 has much larger errors in the lift and drag coefficients than CG21. In more detail, Fig. 17 compares the lift and drag values for grids of CG1, CG21, and CG32. Figure 17 shows that CG32 match well with CG21 and CG1 data at small angles of attack; however, for angles above 6 deg, CG32 lift overestimates CG21/CG1 data, and CG32 underestimates drag. Finally, for the structured grids of CG11, CG20, and CG21, Table 2 shows that the accuracy is improved by decreasing $y^+$ from 1 to 0.26; this, however, does not

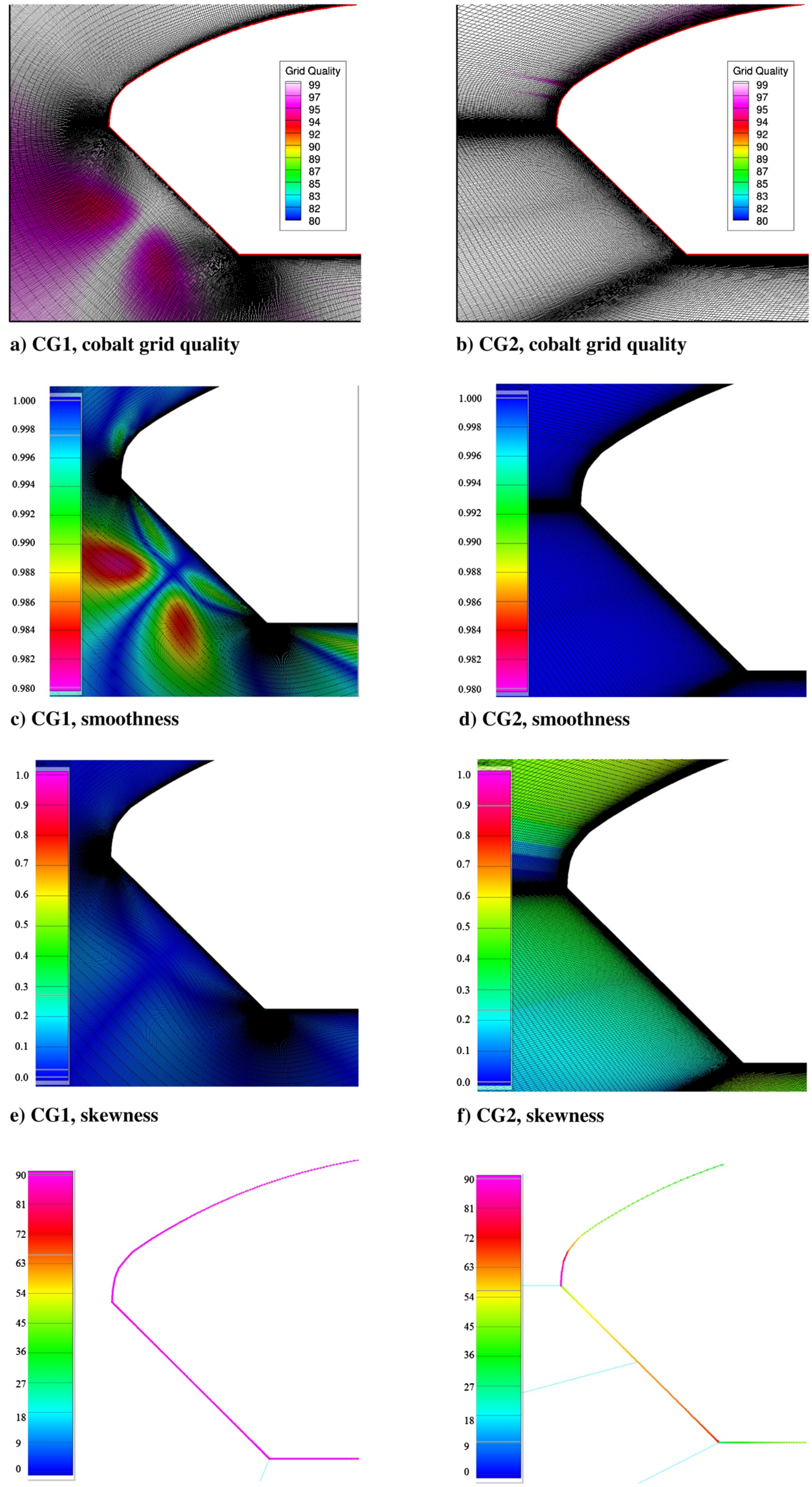


a) CG1, cobalt grid quality

b) CG2, cobalt grid quality

c) CG1, smoothness

d) CG2, smoothness

e) CG1, skewness

f) CG2, skewness

g) CG1, wall orthogonaliy (deg)

h) CG2, wall orthogonaliy (deg)

**Fig. 10 Cobalt grid quality relationship with grid geometry; grid is around leading edge. In Figs. 10a and 10b, the white cells have the highest quality.**

apply to the unstructured grids. Decreasing the initial spacing makes the cells near the wall more skewed assuming the wall spacing is unchanged. Poor skewness would impact the solution accuracy.

The final closed grids considered are of hybrid type with prismatic layers near the wall and isotropic cells elsewhere. Three hybrid grids CG40, CG41, and CG42, were generated. The prismatic layers were generated by the wall normal extrusion using an elliptic solver. The outer domain is then gridded by the Delaunay tetrahedralization. These grids are much coarser than the structured grids of CG10 to CG21. Grid details and errors are again given in Tables 1 and 2. The main difference between these grids is the number of prism layers. Figure 18 shows the grid overview of CG42 with 75 prism layers. The effect of the number of prism layers on the errors can be seen in Fig. 19, which shows that the accuracy is significantly improved by

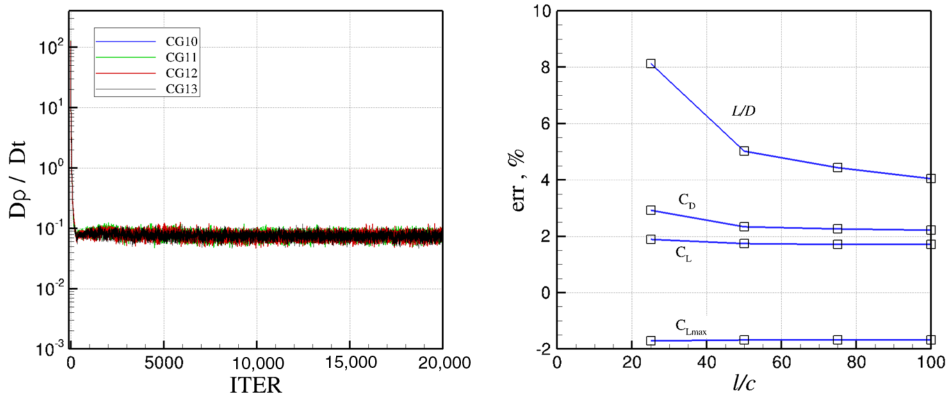


a) Density residuals b) Errors

**Fig. 11 Effects of far-field length $l$ on the solution convergence and errors.**

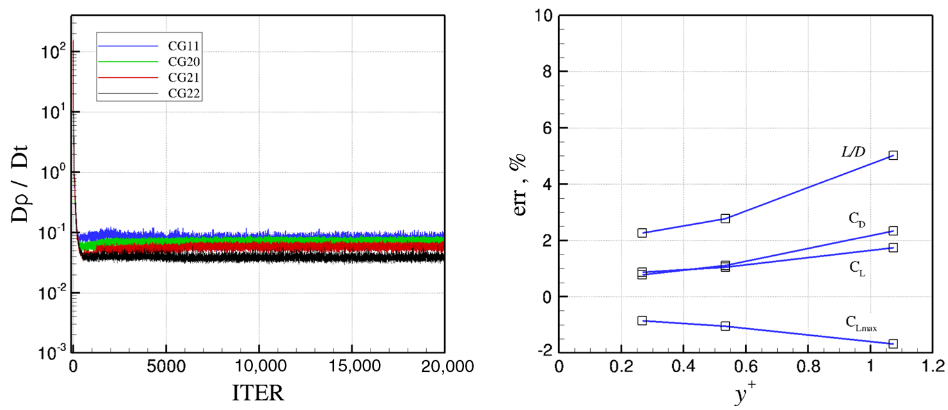


a) Density residuals b) Errors

**Fig. 12 Effects of initial grid spacing $\Delta_{s1}$ on the solution convergence and errors of structured grids.**

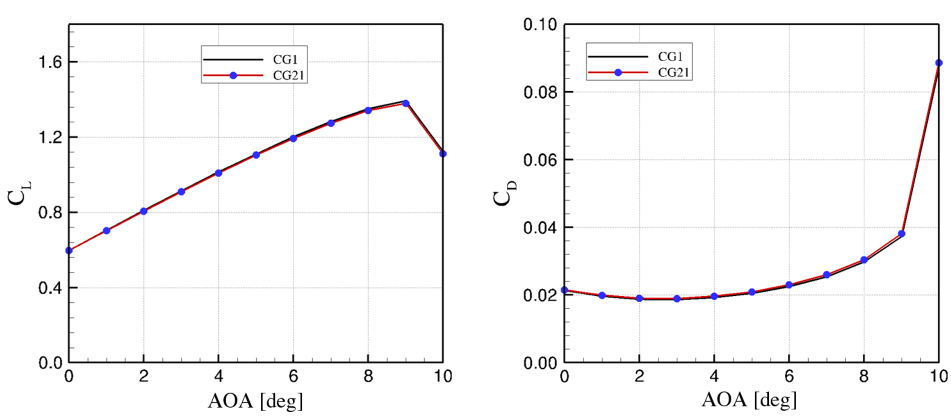


a) Lift coefficient b) Drag coefficient

**Fig. 13 Lift and drag coefficients of CG1 (341,850 cells) and CG21 (133,920 cells) grids.**

increasing the layers from 25 to 50; however, the accuracy does not change much by increasing layers from 50 to 75. Figure 20 also compares the lift and drag coefficients of the hybrid CG42 grid with predictions of CG1 and CG21 grids. The results show that predictions from a hybrid grid with 75 prism layers still match quite well with expected data.

Finally, Fig. 21 shows the flow solution on the CG1, CG2, CG32, and CG42 grids at 9 deg angle of attack. For all grids at $\alpha = 9$ deg, the boundary layer is separated from the upper surface, and a clockwise-rotating eddy is formed. Figure 21 shows that eddy size and pressure coefficients are very similar for the CG1 and CG42 grids; these grids have well-shaped cells with 90 deg wall angles close to the wall. Eddies predicted by the CG2 and CG32 are, however, bigger and smaller than the CG1 eddy, respectively. Therefore, CG2 underestimates and CG32 overestimates the lift predicted by CG1. Note that the CG2 is a structured grid with poor skewness and wall orthogonality; CG32 has highly skewed tetrahedral cells at the wall as well.

### B. Open-Inlet Airfoil

The computational domain of this geometry may be considered to have two parts corresponding to the outside and inside of the airfoil. These domains are gridded separately in this work. Open grid details are given in Table 3. The first grids considered are structured; the outside grid was generated by the wall normal extrusion, and the

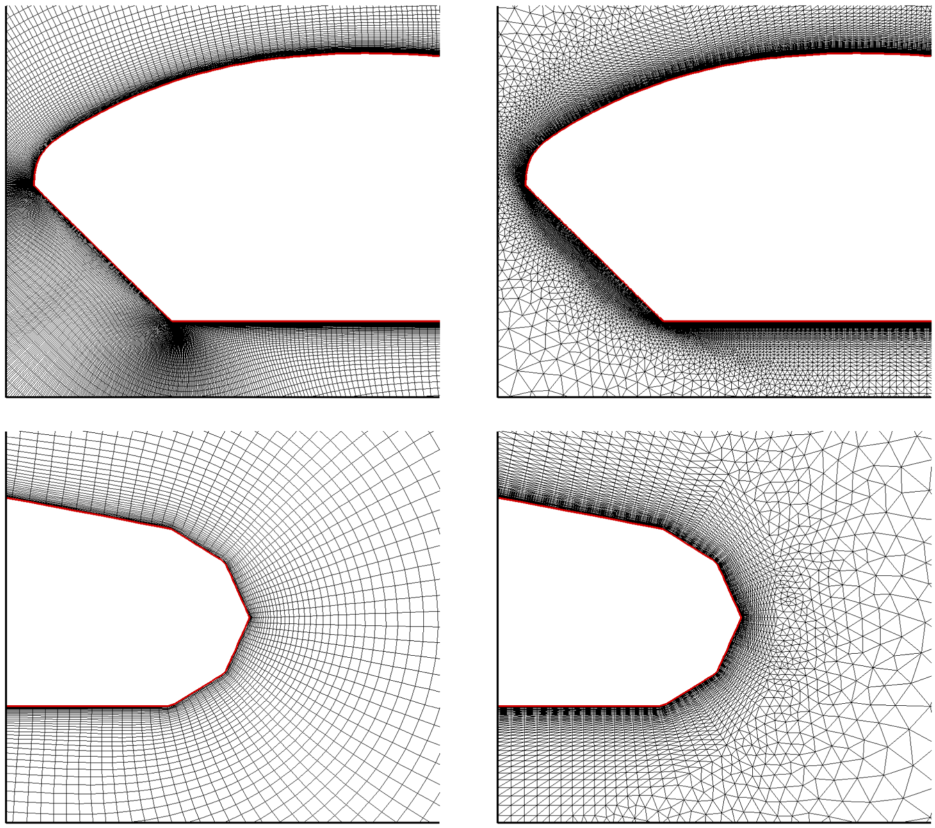

a) CG21, STR, elliptic grid

b) CG32, UNSTR with anisotropic viscous layers

**Fig. 14 CG21 and CG32 grids overview.**

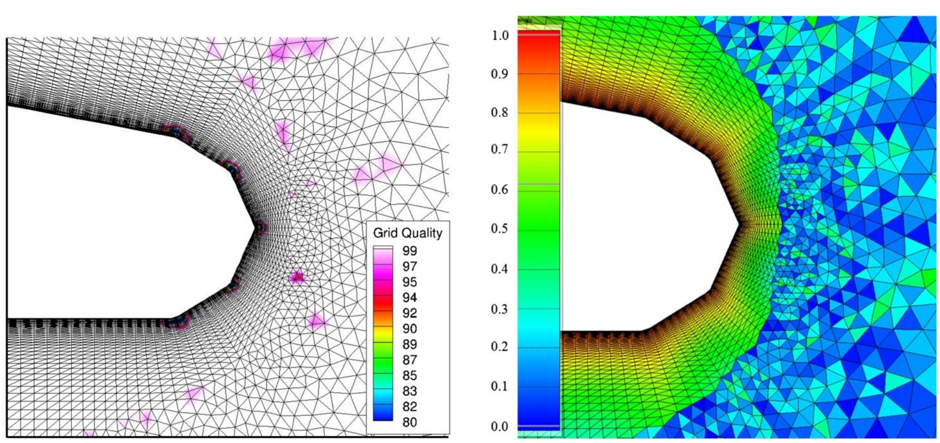


a) Cobalt grid quality

b) Skewness

**Fig. 15 Cobalt cell quality vs the cell skewness report of CG32 grid.**

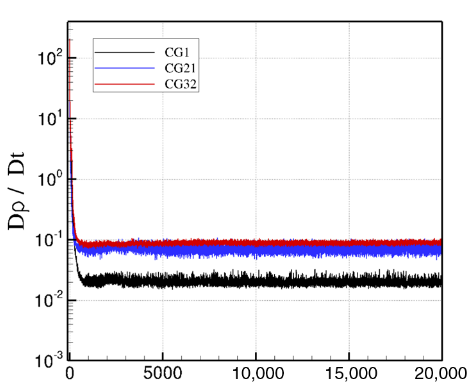


**Fig. 16 Density residual convergence ($D\rho/Dt$) of CG1 (STR with 341,850 cells), CG21 (STR with 133,920 cells), and CG32 (UNSTR with 128,564 cells).**

inside grid is an algebraic grid nearly uniform in spacing even at the inside walls. These grids are named OG1–OG5. All these grids have the same inside grid containing approximately 278,000 cells. OG1–OG3 have an initial spacing of $4 \times 10^{-5}$ m at the outside walls, but the number of layers of constant spacing is different. OG4 and OG5 have five layers of constant spacing at the outside walls, but the initial spacing of these grids is $2 \times 10^{-5}$ and $1 \times 10^{-5}$ m, respectively. The OG1 grid is shown in Fig. 22. OG1 has 25 layers of constant spacing at the outside walls, which can easily be seen in Fig. 22.

OG1 to OG5 grids contain around 400,000 cells. Figure 23a shows the convergence histories of OG1, OG2, and OG3 grids compared with the hybrid fine ("Hfine") grid (1.7 million cells) convergence. The convergence comparisons show that all coarse grids converged to the same values, again due to having similar resolution and quality, and do differ significantly from the Hfine converged value. In comparison to the closed-inlet airfoil convergence plots, Fig. 23a

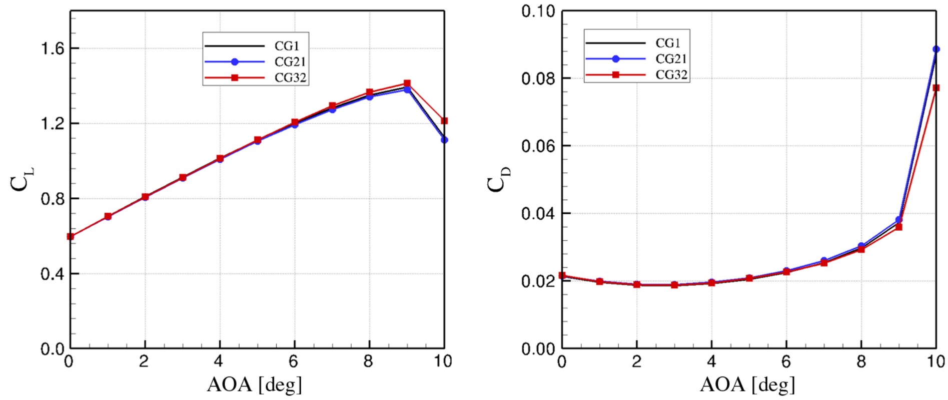


a) Lift coefficient b) Drag coefficient

**Fig. 17 Lift and drag coefficients of CG1, CG21, and CG32.**

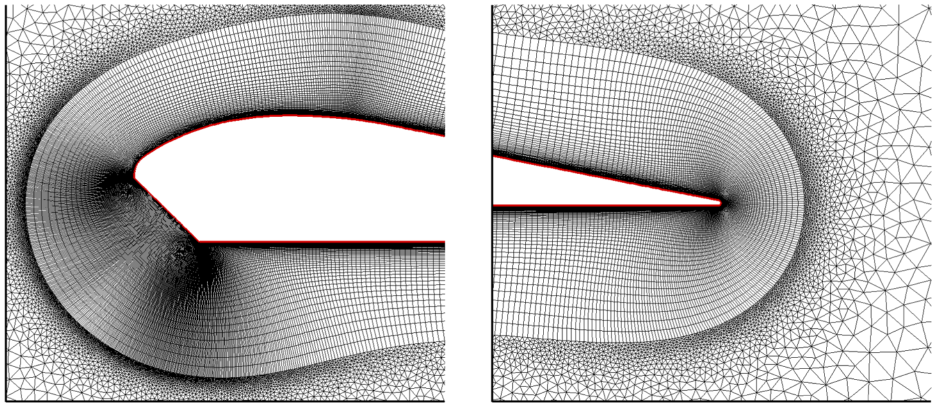

**Fig. 18 Hybrid grid of CG42 with 75 prismatic layers near the wall.**

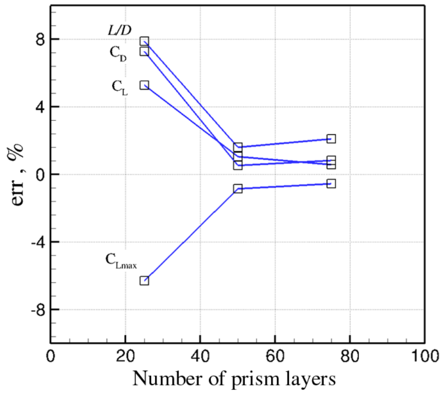


**Fig. 19 Solution errors against number of prism layers in the hybrid grids.**

shows that the open inlet takes a longer time to converge with the Hfine grid having the quickest convergence.

The effects of the number of constant-spacing layers at the wall ($N_s$) on the errors are shown in Fig. 23b. The results show that $N_s$ has a small effect on the open-inlet solutions. The lift and drag coefficients of OG1, OG2, and OG3 grids are compared with the fine grid predictions in Fig. 24. The lift and drag coefficients are split into the inner and outer surfaces. Notice that inner lift does not change with the angle of attack; Ghoreyshi et al. [21] showed that flow is relatively stationary inside, with $C_p$ near 1 almost everywhere. For an open-inlet geometry, when the pressure integral over the outer surface is completed, a negative drag is resolved, which is opposed to the drag formed over the closed-inlet geometry. The comparison plots of Fig. 24 show that coarse grids with uniform spacing inside match

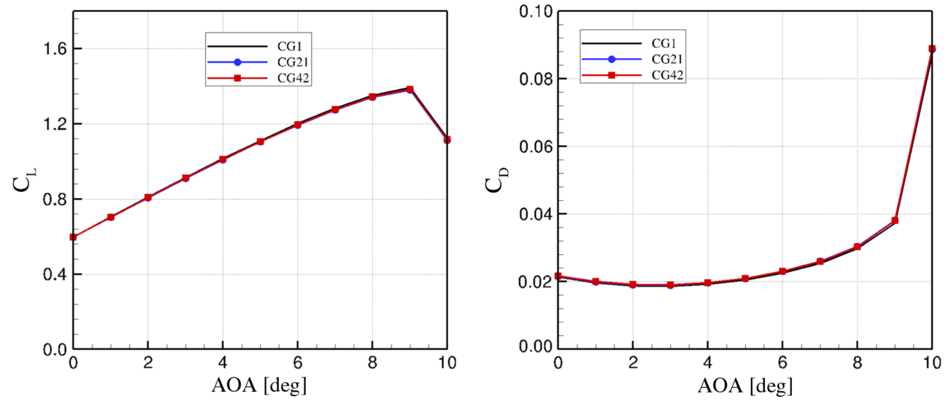


a) Lift coefficient b) Drag coefficient

**Fig. 20 Lift and drag coefficients of CG42 grid.**

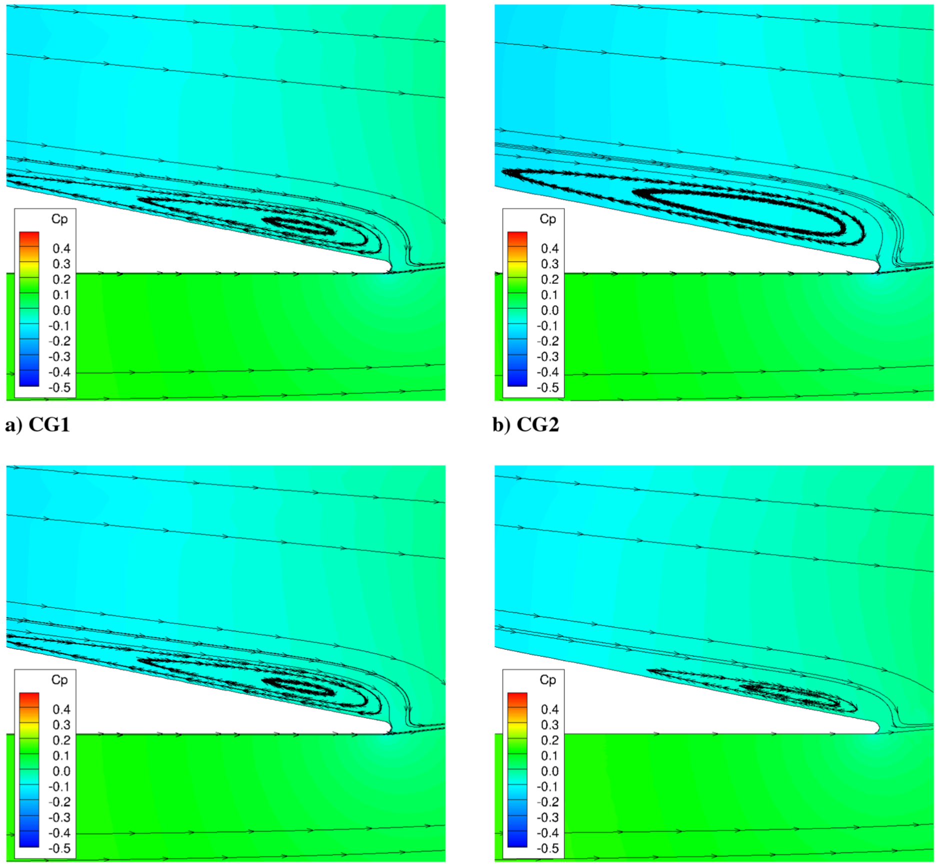


a) CG1 b) CG2

c) CG42 d) CG32

**Fig. 21 Flow solutions of CG1, CG2, CG32, and CG42 grids at $\alpha = 9$ deg.**

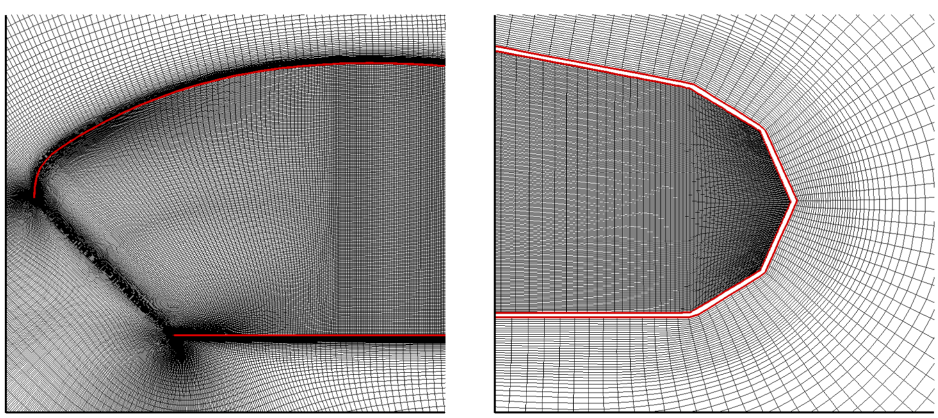

**Fig. 22 OG1 grid overview.**

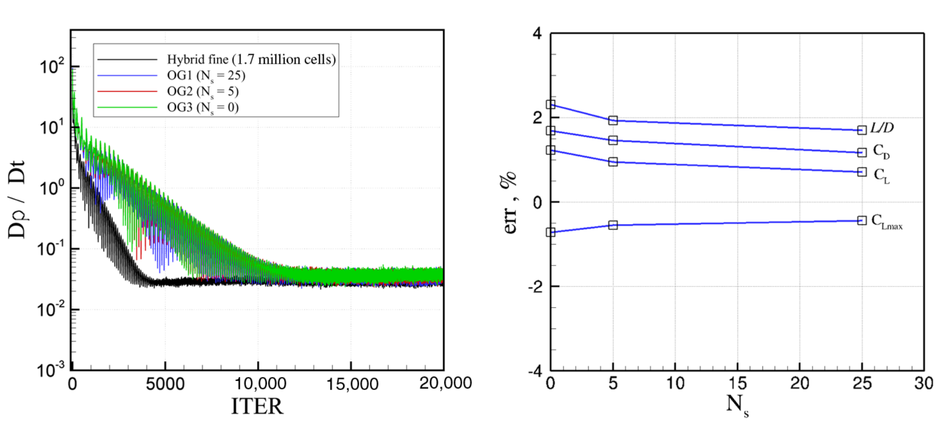


a) Density residuals b) Errors

**Fig. 23 Effects of initial grid spacing $N_s$ on the solution convergence and errors of open airfoil grids. These plots and those of Fig. 24 include results with the hybrid fine grid (1.7 million cells) of [21].**

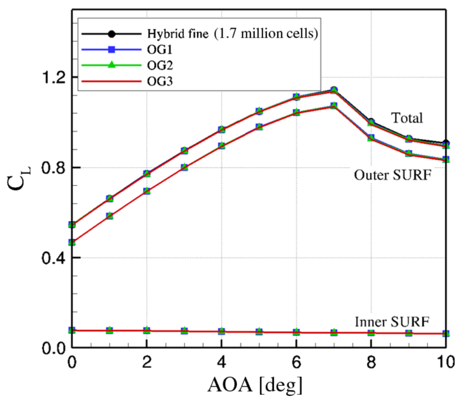


a) Lift coefficient

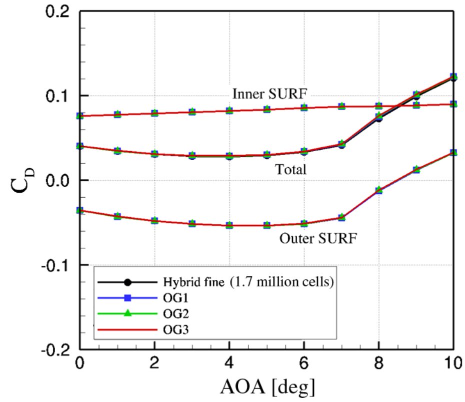


b) Drag coefficient

**Fig. 24 Lift and drag coefficients of OG1, OG2, and OG3.**



very well with the fine grid force coefficients at inside and outside walls.

OG2, OG4, and OG5 have approximately 278,000 cells inside and very similar grids outside; in these grids, $N_s = 5$, and the growth rate is 1.1. However, the initial grid spacing is different; $y^+$ values of these grids are given in Table 4 and range from 1 for the OG2 to 0.23 for the OG5. The effects of $y^+$ on the errors are shown in Fig. 25 and compared with trends of closed-inlet solutions. Figure 25 shows that the errors of the open-inlet grids are slightly reduced by decreasing $y^+$; however, the errors for all $y^+$ values considered are small and less than 2%. On the other hand, the solution accuracy of the closed-inlet grid significantly changes with $y^+$. A possible explanation of why the open-inlet geometries are less sensitive to $y^+$ than closed-inlet can be offered from the flow solutions. Figure 26a shows the flow streamlines of OG5 grid at $\alpha = 9$ deg. At moderate to high angles of attack, flow enters the open section of the open-inlet and then exits from the upper and lower surfaces. This makes flow separated over the upper and lower surface right at the inlet. The closed-inlet geometry at high angles of attack also shows a separated flow region right at the inlet due to the inlet sharp angle; however, the separated region is significantly smaller than those occurred on the open-inlet airfoils. In the closed inlet, the separated eddy size largely depends on the predicted boundary layer at the inlet wall surface; this makes the flow solutions very sensitive to the initial grid spacing and viscous layer used at the inlet surface.

The OG5, OG10, OG11, and OG12 grids were used to study the effect of inside grid resolution on the overall solutions. All these grids have very similar grids outside, but inside grid changes from 278,000 to 22,000 cells. This is achieved by reducing the inside wall grid dimensions. The OG12 grid is shown against OG5 in Fig. 27. Figure 28a shows that the density residual on the OG12 (coarse grid) is not reduced as low as OG5 and the fine grid; however, the accuracy is still as good as others as shown in Fig. 28b, which shows OG12 errors from the fine grid are less than 1%. This means that the open-inlet solution is not very sensitive to the number of cells inside.

To investigate the inside grid type on the solution, OG20 and OG21 grids were also generated; these grids again have a structured grid outside as the previous grids, but the inside was gridded by the Delaunay tetrahedralization. OG20 has only 9800 tetrahedra cells inside; the grid is shown in Fig. 29a. Table 1 and Fig. 30 show that OG20 with coarse tetrahedra cells inside still match with the fine data. Therefore, solutions do not depend much on the inside cell resolution or cell type. Figure 26b shows the flow solutions of OG20 at $\alpha = 9$ deg. This figure shows that the flow inside the airfoil is stationary almost everywhere, as predicted by other grids; therefore, the flow solution should not change much with inside grid resolution.

**Table 4 Open grid solution details**

| Grid | $y^+$ | Quality | Error, % $C_L$ | $C_D$ | $L/D$ | $C_{L\max}$ |
|---|---|---|---|---|---|---|
| HFine | 0.0656 | 99.83 | — — | — — | — — | — — |
| OG1 | 0.9490 | 99.66 | 0.7146 | 1.1728 | 1.7029 | −0.4407 |
| OG2 | 0.9495 | 99.69 | 0.9527 | 1.4604 | 1.9284 | −0.5427 |
| OG3 | 0.9501 | 99.70 | 1.2356 | 1.6935 | 2.3153 | −0.7218 |
| OG4 | 0.4721 | 99.66 | 0.4549 | 0.5146 | 0.5746 | −0.1788 |
| OG5 | 0.2360 | 99.59 | 0.4232 | 0.3767 | 0.4536 | −0.1312 |
| OG10 | 0.2360 | 99.26 | 0.4269 | 0.3506 | 0.4322 | −0.0934 |
| OG11 | 0.2359 | 98.85 | 0.4430 | 0.4462 | 0.5599 | −0.1770 |
| OG12 | 0.2357 | 98.86 | 0.5402 | 0.4694 | 0.8619 | −0.4866 |
| OG20 | 0.2360 | 98.92 | 0.4994 | 1.5627 | 2.6723 | −0.1016 |
| OG21 | 0.2360 | 98.91 | 0.4323 | 1.8874 | 3.8378 | −0.1263 |
| OG22 | 0.1599 | 99.35 | 3.4452 | 1.1538 | 2.6855 | 1.7791 |
| OG40 | 0.2364 | 98.90 | 1.0078 | 1.5233 | 3.2509 | 0.3833 |

**Table 3 Open grid detail ($l/c = 100$ and GR $= 1.1$ for all grids)**

| Grid | Outside grid | Inside grid | $\Delta_{s1}$ | $N_s$ | Number of cavity cells | Number of total cells |
|---|---|---|---|---|---|---|
| HFine | Hybrid | Hybrid | 1e − 5 | — — | — — | 1,782,199 |
| OG1 | STR, elliptic | STR, uniform | 4e − 5 | 25 | 278,620 | 421,840 |
| OG2 | STR, elliptic | STR, uniform | 4e − 5 | 5 | 278,620 | 403,240 |
| OG3 | STR, elliptic | STR, uniform | 4e − 5 | 0 | 278,620 | 399,520 |
| OG4 | STR, elliptic | STR, uniform | 2e − 5 | 5 | 278,620 | 407,500 |
| OG5 | STR, elliptic | STR, uniform | 1e − 5 | 5 | 278,620 | 416,260 |
| OG10 | STR, elliptic | STR, uniform | 1e − 5 | 5 | 120,384 | 285,028 |
| OG11 | STR, elliptic | STR, uniform | 1e − 5 | 5 | 56,000 | 194,188 |
| OG12 | STR, elliptic | STR, uniform | 1e − 5 | 5 | 22,000 | 148,262 |
| OG20 | STR, elliptic | UNSTR | 1e − 5 | 5 | 9,812 | 137,058 |
| OG21 | STR, elliptic | UNSTR | 1e − 5 | 5 | 5,209 | 136,520 |
| OG22 | UNSTR | UNSTR | 1e − 5 | — — | 5,275 | 118,202 |
| OG40 | Hybrid | UNSTR | 1e − 5 | — — | 5,275 | 98,620 |

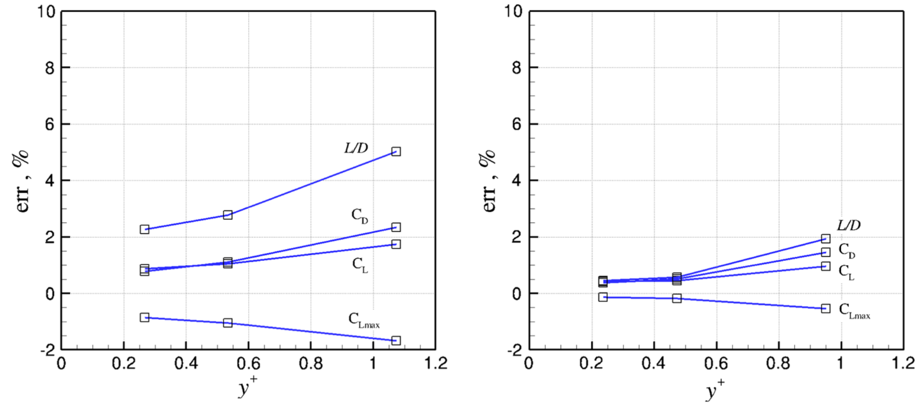


a) Closed inlet

b) Open inlet

**Fig. 25 Effects of initial grid spacing $\Delta_{s1}$ on the solution errors of closed- and open-inlet grids.**

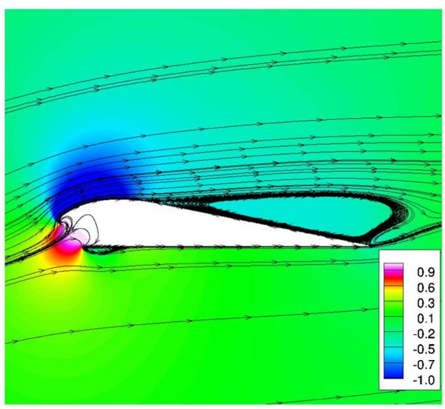

**a) OG5**

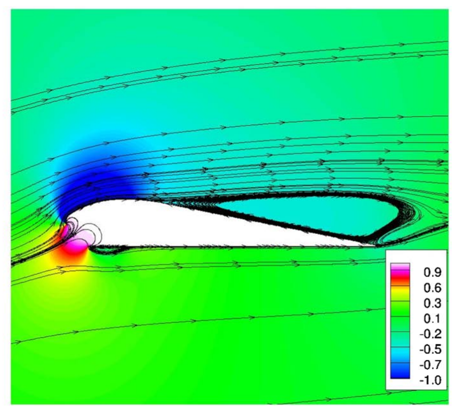

**b) OG20**

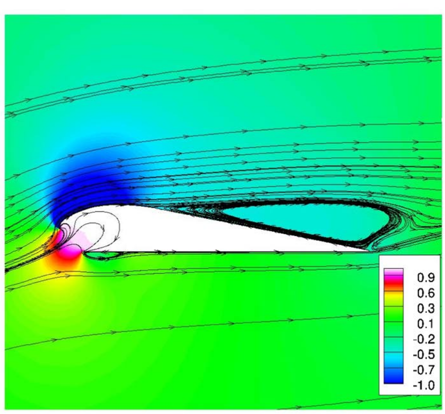

**c) OG22**

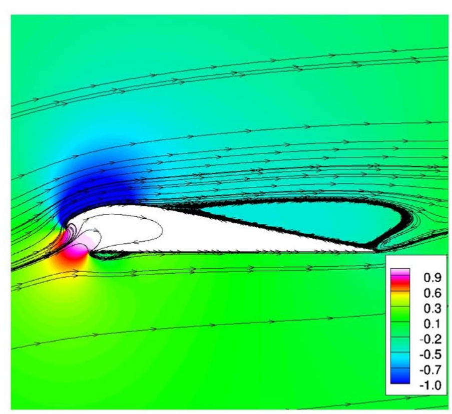

**d) OG40**

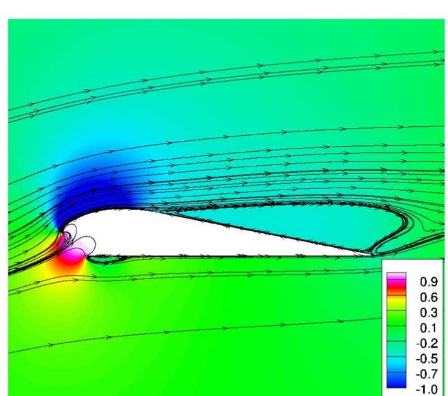

**e) HFine grid**

**Fig. 26 Flow solutions of OG5, OG20, OG22, and OG40 grids at $\alpha = 9$ deg. The time-averaged pressure coefficients $C_p$ are shown.**

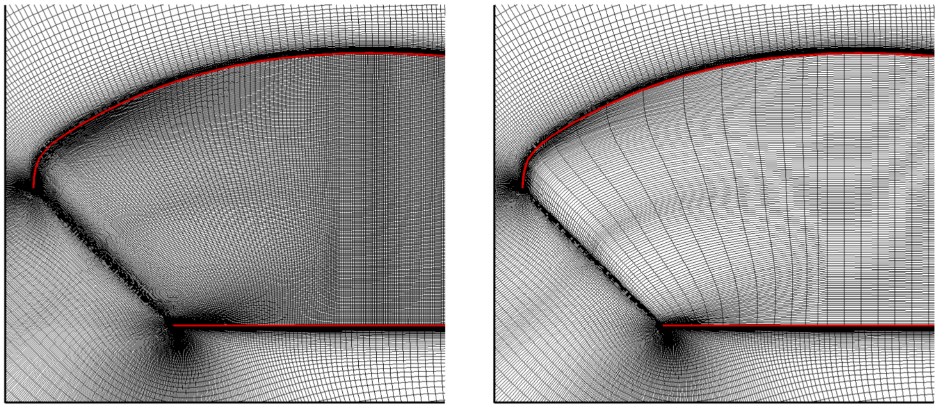

a) OG5 b) OG12

Fig. 27 OG5 (with 410,260 cells) grid overview compared to OG12 (with 148,262 cells).

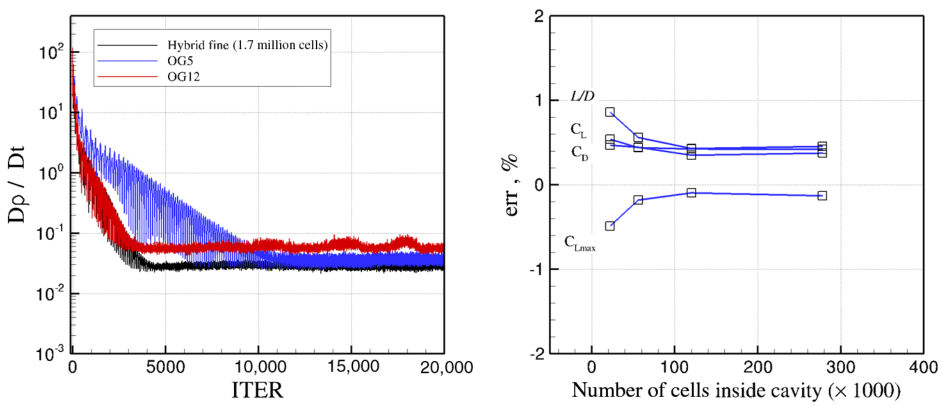


a) Density residuals b) Errors

Fig. 28 Effects of cavity cell numbers on the solution convergence and errors of open airfoil grids.

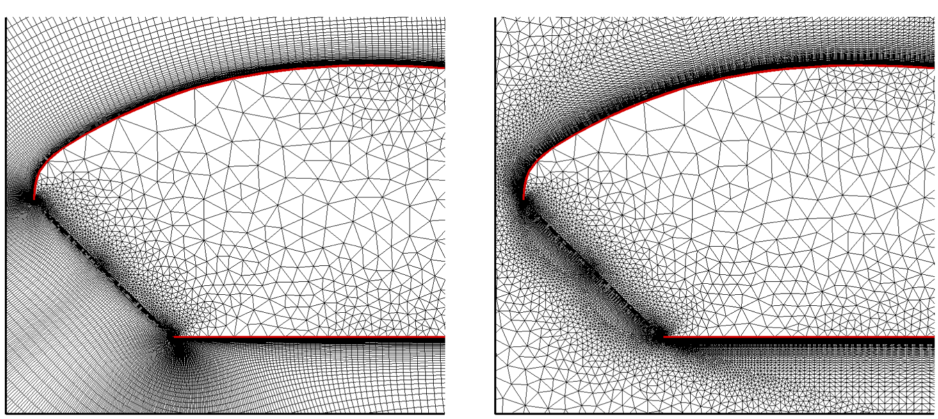

a) OG20 b) OG22

Fig. 29 Overview of OG20 and OG22 grids.

The OG22 grid has unstructured cells inside and outside. The outside is gridded by the Delaunay tetrahedralization and has anisotropic layers at the wall. Inside cells are isotropic tetrahedra cells. The grid and solutions are shown in Figs. 29b and 30, respectively. Figure 30 shows that the forces on the outer surface of the airfoil and therefore total lift and drag do not match with Hfine data everywhere. This is probably due to having highly skewed tetrahedral cells near the outer walls. The flow solution on the OG22 grid is also shown in Fig. 26c for $\alpha = 9$ deg. The figure shows that the flow is separated from the upper surface, and a clockwise-rotating eddy is formed at this angle; however, the eddy size and septation do not match with those predicted by OG5 and OG20 grids. Note that the eddy formed over the open-inlet airfoil is much bigger than those predicted over the closed-inlet airfoil at $\alpha = 9$ deg.

The final grid, OG40, is a hybrid grid outside and unstructured inside. The viscous grid on the outside wall was generated by the wall normal extrusion; it has 75 layers. The rest of the outside domain is gridded by the Delaunay grid generator. An overview of the grid is shown in Fig. 31. The convergence solution on this grid is plotted in Fig. 32, which shows that the residual reduction for the OG40 and OG20 grids are the same; however, residual reduction of these grids is not as low as OG1 or the fine grid. On the other hand, the OG20 grid (with unstructured cells inside) and OG40 hybrid grid exhibit a faster convergence rate than the OG1 structured grid. The lift and drag

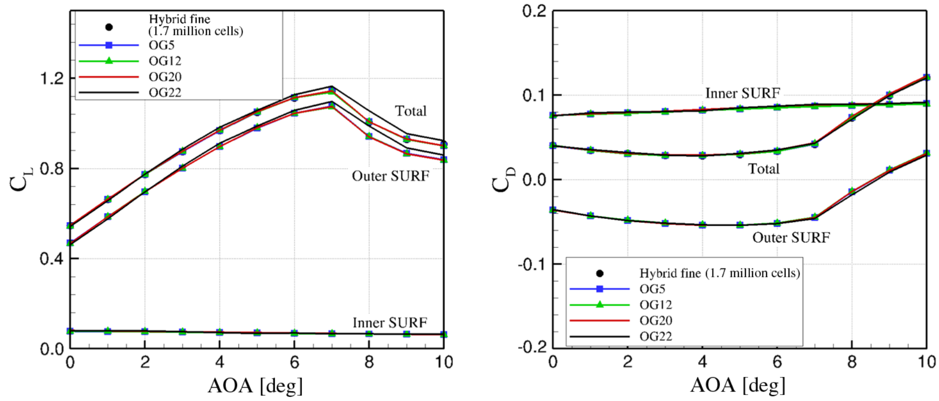


a) Lift coefficient b) Drag coefficient

**Fig. 30 Lift and drag coefficients of OG5, OG12, OG20, and OG22.**

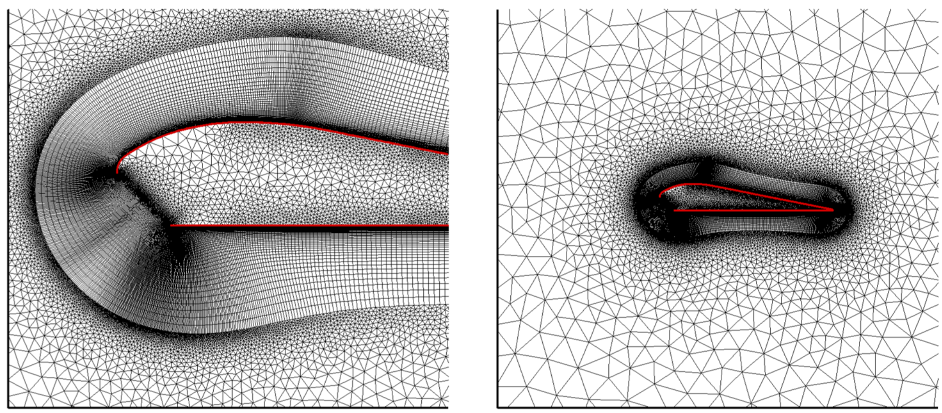

**Fig. 31 OG40 grid overview.**

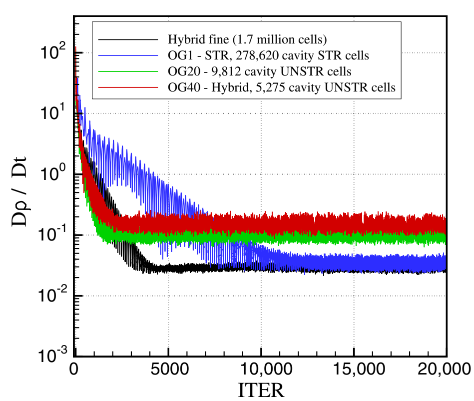


**Fig. 32 Density residual on the OG1, OG20, and OG40 grid as well as the Hfine grid.**

coefficients of the OG40 are also compared with the fine and OG1 grid in Fig. 33, which shows that the hybrid grid matches well with data from the other grid data; there are very small discrepancies in lift coefficients in the poststall region. Figure 26d shows the flow solution over this grid at $\alpha = 9$ deg. Note that the eddy size at this angle is bigger than the viscous layer generated with 75 prismatic layers; this probably explains the small discrepancies between this grid and those of the structured type.

## VI. Conclusions

This work provides an overview of the grid quality and resolution effects on the aerodynamic modeling of ram-air parachute canopies. The computational fluid dynamics simulations were performed using the Cobalt flow solver on two-dimensional canopy sections with open and closed inlets. The simulation results show that Cobalt grid quality (ranging from zero to 100) depends mainly on the grid

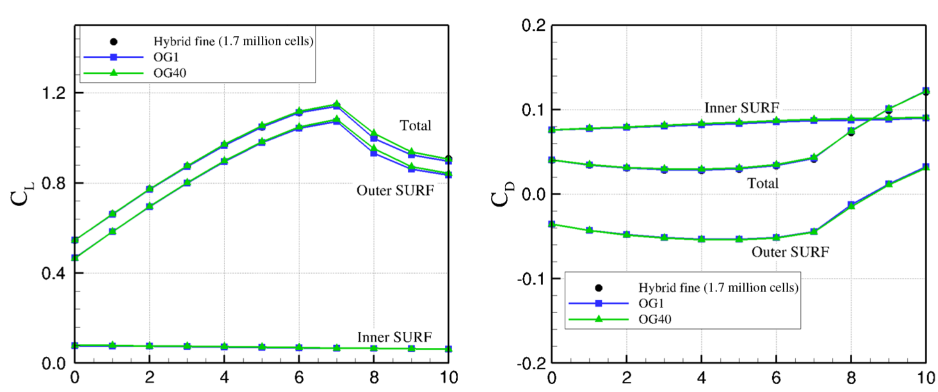


a)Lift coefficient b) Drag coefficient

**Fig. 33 Lift and drag coefficients predicted by the hybrid OG40 grid.**

smoothness but not the skewness or the wall orthogonality. Increasing the grid resolution and grid quality (smoothness) and decreasing the initial grid spacing at the wall ($y^+$) helps to reduce the density residual magnitude. The results showed that, although a high quality grid of Cobalt leads to a better convergence, it does not always lead to a better accuracy. The solution accuracy will change with grid resolution and smoothness as well as skewness and the wall orthogonality.

The results of this work showed that the solutions of coarse structured and hybrid grids (around 100,000 cells) can match well with prediction of fine grids containing a few million cells. These coarse grids have appropriate $y^+$ values, good smoothness, skewness, and wall orthogonality. Although unstructured grids with anisotropic cells near the wall have very good grid quality in Cobalt, they have the worst accuracy between considered grids because of poor skewness at the walls. The results also showed that, in comparison to the closed inlets, the open geometry solutions are less sensitive to the initial grid spacing and number of constant spacing layer at the outside walls. Also, the solutions do not change with inside grid resolution and type. However, a grid with anisotropic layers at the outside walls has again the worst accuracy between considered grids.

Results from this research, which included three different topologies (structured, unstructured, and hybrid) applied to both closed and open airfoil geometries, suggest several best practices to follow for creating efficient viscous grids. A computational domain with a radius of approximately 50 chord lengths produced accurate values for $L/D$, the figure of merit. Cell skewness has a dramatic effect on accuracy with an order of magnitude decrease in $L/D$ between the structured girds, CG1 (normal extrusion, elliptic) and CG2 (multiblock, algebraic). Skewness is especially important for the grid elements near a wall boundary. To resolve boundary layers, 1) use a geometry-conforming mesh with good wall orthogonality; 2) select a $y+$ no greater than 1, but residuals converged twice as fast for $y+\approx 0.25$; and 3) smoothness, as measure by growth rate of the grid elements, should be no more than 1.2, with 1.1 yielding the best resolution when coupled to at least 50 prism layers (greater than 50 layers only resulted in marginally better solutions).

Although these recommendations often reinforce results seen in previous research, the application to both the closed and open airfoils provided additional insight. In particular, the open geometries are not as sensitive to the dependence on $y+$. Additionally, because of quiescent flow inside the open inlet geometry, a greatly reduced resolution may be used. For future 3-D simulations, in which there will be between seven and 20 open-inlet airfoil sections, the computational savings will be substantial.

## Acknowledgments

Mehdi Ghoreyshi and Jürgen Seidel are supported by the U.S. Air Force Academy (USAFA); their financial support is gratefully acknowledged. Acknowledgments are expressed to the Department of Defense High Performance Computing Modernization Program and the Engineering Research Development Center for providing computer time. The authors appreciate the support provided by the Natick Soldier Research Development and Engineering Center Airdrop Technology Team and the High Performance Computing Research Center at USAFA. This material is based in part on research sponsored by the USAFA under agreement number FA7000-13-2-0009.

## References

[1] Anderson, J. D., *Modern Compressible Flow*, 2nd ed., McGraw–Hill, New York, 1990, pp. 309–310.
[2] McCormick, S. F., *Multilevel Adaptive Methods for Partial Differential Equations*, Soc. of Industrial and Applied Mathematics, Philadelphia, 1989, pp. 102–103.
[3] Gu, X., Schock, H. J., Shih, T. I.-P., Hernandez, E. C., Chu, D., Keller, P. S., and Sun, R. L., "Grid-Quality Measures for Structured and Unstructured Meshes," *39th Aerospace Sciences Meeting and Exhibit*, AIAA Paper 2001-0652, Jan. 2001.
[4] Thompson, J. F., Soni, B. K., and Weatherill, N. P., *Handbook of Grid Generation*, CRC Press, Boca Raton, FL, 1999, pp. 25-1–25-14.
[5] Liseikin, V. D., *Grid Generation Methods (Scientific Computation)*, 2nd ed., Springer, London, 2010, pp. 2–3.
[6] Knupp, P., and Steinberg, S., *Fundamentals of Grid Generation*, CRC Press, Boca Raton, FL, 1994, pp. 155–156.
[7] Henne, P. A., *Applied Computational Aerodynamics*, AIAA, Washington, D.C., 1990, pp. 9-2–9-3.
[8] Baker, T. J., "Three Decades of Meshing; A Retrospective View," *16th AIAA Computational Fluid Dynamics Conference*, AIAA Paper 2003-3563, June 2003.
[9] Ali, Z., and Tucker, P. G., "Multiblock Structured Mesh Generation for Turbomachinery Flows," *Proceedings of the 22nd International Meshing Roundtable*, Springer, Berlin, 2014.
[10] Cheng, S.-W., Dey, T. K., and Shewchuk, J. R., *Delaunay Mesh Generation*, CRC Press, Boca Raton, FL, 2013, pp. 10–27.
[11] Leondes, C. T., *Structural Dynamic Systems Computational Techniques and Optimization*, Vol. 52, Gordon and Breach Science Publ., Amesterdam, 1998, pp. 149–200.
[12] Michal, T., and Cary, A., "Unstructured Grid Extrusion for Viscous Flow Simulations," *39th Aerospace Sciences Meeting and Exhibit*, AIAA Paper 2001-0444, Jan. 2001.
[13] Chalasani, S., and Thompson, D., "Quality Improvements in Extruded Meshes Using Topologically Adaptive Generalized Elements," *International Journal for Numerical Methods in Engineering*, Vol. 60, No. 6, 2004, pp. 1139–1159. doi:10.1002/(ISSN)1097-0207
[14] Ito, Y., and Nakahashi, K., "Unstructured Hybrid Grid Generation Based on Isotropic Tetrahedral Grids," *40th AIAA Aerospace Sciences Meeting and Exhibit*, AIAA Paper 2002-0861, Jan. 2002.
[15] Ghoryeshi, M., Jirasek, A., and Cummings, R. M., "Computational Investigation into the Use of Response Functions for Aerodynamic Loads Modeling," *AIAA Journal*, Vol. 50, No. 6, 2012, pp. 1314–1327. doi:10.2514/1.J051428
[16] Ghoryeshi, M., Post, M. L., and Cummings, R. M., "CFD Calculation of Aerodynamic Indicial Functions for a Generic Fighter Configuration," *ITEA Journal of Test and Evaluation*, Vol. 33, No. 6, 2012, pp. 348–364.
[17] Ghoreyshi, M., Cummings, R. M., DaRonch, A., and Badcock, K. J., "Transonic Aerodynamic Loads Modeling of X-31 Aircraft Pitching Motions," *AIAA Journal*, Vol. 51, No. 10, 2013, pp. 2447–2464. doi:10.2514/1.J052309
[18] Ghoreyshi, M., and Cummings, R. M., "Unsteady Aerodynamics Modeling for Aircraft Maneuvers: A New Approach Using Time-Dependent Surrogate Modeling," *Aerospace Science and Technology*, Vol. 39, Dec. 2014, pp. 222–242. doi:10.1016/j.ast.2014.09.009
[19] Tyssel, L., "Hybrid Grid Generation for Complex 3D Geometries," *Proceedings of the 7th International Conference on Numerical Grid Generation in Computational Field Simulation*, 2000, International Soc. of Grid Generation ( ISGG ), New York, pp. 337–346.
[20] Tyssel, L., "The TRITET Grid Generation System," *Proceedings of the 10th International Conference on Numerical Grid Generation in Computational Field Simulations*, International Soc. of Grid Generation ( ISGG ), New York, 2007.
[21] Ghoreyshi, M., Seidel, J., Bergeron, K., Jirasek, A., Lofthouse, A. J., and Cummings, R. M., "Prediction of Aerodynamic Characteristics of a Ram-Air Parachute," *32nd AIAA Applied Aerodynamics Conference*, AIAA Paper 2014-2831, June 2014.
[22] Bergeron, K., Jurgen, S., Ghoreyshi, M., Jirasek, A., Lofthouse, A. J., and Cummings, R. M., "Numerical Study of Ram Air Airfoils and Upper Surface Bleed-Air Control," *32nd AIAA Applied Aerodynamics Conference*, AIAA Paper 2014-2832, June 2014.
[23] Strang, W. Z., Tomaro, R. F., and Grismer, M. J., "The Defining Methods of Cobalt: A Parallel, Implicit, Unstructured Euler/Navier–Stokes Flow Solver," *37th Aerospace Sciences Meeting and Exhibit*, AIAA Paper 1999-0786, Jan. 1999.
[24] Gottlieb, J. J., and Groth, C. P. T., "Assessment of Riemann Solvers for Unsteady One-Dimensional Inviscid Flows of Perfect Gasses," *Journal of Computational Physics*, Vol. 78, No. 2, 1988, pp. 437–458. doi:10.1016/0021-9991(88)90059-9
[25] Tomaro, R. F., Strang, W. Z., and Sankar, L. N., "An Implicit Algorithm for Solving Time Dependent Flows on Unstructured Grids," *35th Aerospace Sciences Meeting and Exhibit*, AIAA Paper 1997-0333, 1997.
[26] Tomaro, R. F., Strang, W. Z., and Wurtzler, K. E., "Can Legacy Codes Scale on Tens of Thousands of PEs or Do We Need to Reinvent the Wheel?" *2012 High Performance Computing Modernization Program Contributions to DoD Mission Success*, High Performance Computer Modernization Program, Lorton, VA, Sept. 2012, pp. 231–236.

[27] Spalart, P. R., and Allmaras, S. R., "A One Equation Turbulence Model for Aerodynamic Flows," *30th Aerospace Sciences Meeting and Exhibit*, AIAA Paper 1992-0439, Jan. 1992.

[28] Spalart, P. R., and Shur, M. L., "On the Sensitization of Turbulence Models to Rotation and Curvature," *Aerospace Science and Technology*, Vol. 52, No. 5, 1997, pp. 297–302. doi:10.1016/S1270-9638(97)90051-1

[29] Spalart, P. R., Jou, W.-H., Strelets, M., and Allmaras, S. R., "Comments on the Feasibility of LES for Wings, and on a Hybrid RANS/LES Approach," *Proceedings of the 1st AFSOR International Conference on DNS/LES*, Greyden Press, Columbus, OH, 1997, pp. 137–147.

[30] "Cobalt User's Manual," Cobalt Solutions, Springfield, OH, Feb. 2013.

[31] Dannenhoffer, J. F., "Correlation of Grid Quality Metrics and Solution Accuracy for Supersonic Flows," *50th AIAA Aerospace Sciences Meeting*, AIAA Paper 2012-0610, Jan. 2012.

[32] McDaniel, D. R., "Deformation of Viscous CFD Meshes for Aeroelastic and S&C Applications," Ph.D Dissertation, Dept. of Mechanical and Aerospace Engineering, Univ. of Colorado, Colorado Springs, CO, Nov. 2010.

[33] Rumsey, C. L., and Slotnick, J. P., "Overview and Summary of the Second AIAA High Lift Prediction Workshop," *52nd Aerospace Sciences Meeting*, AIAA Paper 2014-0747, Jan. 2014.

[34] Mavriplis, D. J., Vassberg, J. C., Tinoco, E. N., Mani, M., Brodersen, O. P., Eisfeld, B., Wahls, R. A., Morrison, J. H., Zickuhr, T., Levy, D., and Murayama, M., "Grid Quality and Resolution Issues from the Drag Prediction Workshop Series," *46th AIAA Aerospace Sciences Meeting and Exhibit*, AIAA Paper 2008-0930, Jan. 2008.

[35] Maddock, I., Harby, A., Kemp, P., and Wood, P. J., *Ecohydraulics: An Integrated Approach*, Wiley, Oxford, 2013, pp. 50–80.

[36] Alter, S. J., "A Structured-Grid Quality Measure for Simulated Hypersonic Flows," *42nd AIAA Aerospace Sciences Meeting and Exhibit*, AIAA Paper 2004-0612, Jan. 2004.

[37] Morton, S. A., McDaniel, D. R., Sears, D. R., Tillman, B., and Tuckey, T. R., "Kestrel: A Fixed Wing Virtual Aircraft Product of the CREATE Program," *47th AIAA Aerospace Sciences Meeting*, AIAA Paper 2009-0338, Jan. 2009.

[38] Benney, R. J., Krainski, W. J., Onckelinx, C. P., Delwarde, C. C., Mueller, L., and Vallance, M., "NATO Precision Airdrop Initiatives and Modeling and Simulation Needs," NATO Science and Technology Organization, Applied Vehicle Technology Technical Rept. TR RTO-MP-AVT-133, Natick, MA, Oct. 2006.

[39] Bergeron, K., Ward, M., and Costello, M., "Aerodynamic Effects of Parafoil Upper Surface Bleed Air Actuation," *AIAA Atmospheric Flight Mechanics Conference*, AIAA Paper 2012-4737, Aug. 2012.

[40] Marchman, J. F., and Werme, T. D., "Clark-Y Airfoil Performance at Low Reynolds Numbers," *22nd Aerospace Sciences Meeting*, AIAA Paper 1984-0052, Jan. 1984.

[41] Lingard, J. S., "Basic Analysis of Ram-Air Parachute," *Precision Aerial Delivery Systems: Modeling, Dynamics, and Control*, AIAA Education Series, AIAA, Reston, VA, pp. 73–125. doi:10.2514/5.9781624101960.0073.0126

[42] Oberkampf, W., and Roy, C., *Verification and Validation in Scientific Computing*, Cambridge Univ. Press, Cambridge, England, U.K., 2010, pp. 324–325.